CrossMark

ORIGINAL PAPER

Multiscale Computational Homogenization: Review and Proposal of a New Enhanced-First-Order Method

Fermin Otero[1] · Sergio Oller[2,3] · Xavier Martinez[3,4]

Abstract The continuous increase of computational capacity has encouraged the extensive use of multiscale techniques to simulate the material behaviour on several fields of knowledge. In solid mechanics, the multiscale approaches which consider the macro-scale deformation gradient to obtain the homogenized material behaviour from the micro-scale are called first-order computational homogenization. Following this idea, the second-order FE2 methods incorporate high-order gradients to improve the simulation accuracy. However, to capture the full advantages of these high-order framework the classical boundary value problem (BVP) at the macro-scale must be upgraded to high-order level, which complicates their numerical solution. With the purpose of obtaining the best of both methods i.e. first-order and second-order, in this work an enhanced-first-order computational homogenization is presented. The proposed approach preserves a classical BVP at the macro-scale level but taking into account the high-order gradient of the macro-scale in the micro-scale solution. The developed numerical examples show how the proposed method obtains the expected stress distribution at the micro-scale for states of structural bending loads. Nevertheless, the macro-scale results achieved are the same than the ones obtained with a first-order framework because both approaches share the same macro-scale BVP.

1 Introduction

Almost all existing materials around us can be considered heterogeneous structures or composite materials, since they are composed by several phases or components at certain spatial scale of observation. Prediction of the physical and chemical behaviour of such materials is a complicated target. Their properties, also called effective or homogenized properties, fully depend on the internal microstructure which can be different from one to another composite in morphology, volume fraction, and of course, in properties of constituents. The interaction between components, failure of interfaces capacity or damage because of fracture of the constituents must be also considered. Therefore, obtaining a good characterization of composite materials behaviour is in general a complex issue and requires considering suitable and sophisticated methods.

1.1 Review of Multiscale Methods

Within the context of solid mechanics, the pioneering works of Eshelby [20], Hashin [38], Hashin and Shtrikman [39, 40], Hill [42–45], Budiansky [10], Mandel [68] and Gurson [37] have been significant theoretical developments for the estimation of macroscopic properties of heterogeneous materials. Following in time, the asymptotic homogenization theory has been another important milestone for modelling multiphase materials. The method is based on asymptotic expansions of displacement, strain and

✉ Fermin Otero
  fotero@inegi.up.pt

1 Institute of Science and Innovation in Mechanical and Industrial Engineering (INEGI), Rua Dr. Roberto Frias 400, 4200-465 Porto, Portugal

2 Departament d'Enginyeria Civil i Ambiental, ETSECCPB, Technical University of Catalonia, Jordi Girona 1-3, 08034 Barcelona, Spain

3 Centre Internacional de Metodes Numerics en Enginyeria (CIMNE), Gran Capitá s/n, 08034 Barcelona, Spain

4 Departamento de Ciencia e Ingeniería Náutica, FNB, Technical University of Catalonia, Pla de Palau 18, 08003 Barcelona, Spain

stress fields around their corresponding macroscopic values. Through variational principles is obtained a set of boundary value problems. Fundamental contributions to this modelling methodology are the original works of Bensoussan et al. [7] and Sanchez-Palencia [102, 103]. Fish and co-workers presented a generalization of the mathematical homogenization method based on double-scale asymptotic expansion to account for non-linear effects such as plasticity [26] and damage [27] in heterogeneous media. The asymptotic homogenization method was continuously developed and nowadays, it still is a very popular research topic [12, 17, 51, 98, 116].

In the last decade, several multiscale approaches have been developed becoming nowadays in an essential technique for modelling composites materials. This is because, even today performing a full direct numerical simulation including all the heterogeneities leads to a huge problem, which is expensive and unworkable from a computational cost point of view. On the other hand, carrying out numerous experiments on many material samples with different geometrical and physical properties is practically impossible because of time and cost.

In a general sense, it is possible classify the multiscale models into the *concurrent method* [9, 19, 28, 31, 32, 47, 62, 67, 84, 117, 127] and the *homogenization method*, on the latter one will be focused this article. The main feature of a generic concurrent multiscale method is that coarse- and fine-scale regions are processed simultaneously. The links between different scales are accounted considering displacement compatibility and momentum balance across the whole solid. Therefore, this framework considers a strong coupling between the scales. On the other hand, the multiscale homogenization method is based on the principle of separation of scales and then, micro-scale length is assumed much smaller than macro-scale length [30]. Consequently, in this approach the length scales of micro- and macro-problems must be sufficiently separate.

Multiscale homogenization method which uses the concept of Representative Volume Element (RVE) [7, 42, 109, 113, 125] together with suitable computational approaches has emerged as one of the most promising formulation to address the response of composites structures. The RVE is employed to determine the homogenized properties and behaviour of a material point at the macro-scale level. It is defined as a microstructural subregion and must be large enough to be statistically representative of the composite material including all its microscopic heterogeneities [18, 33, 53, 71, 90, 120]. However, it must remain sufficiently small to be considered as a volume element of the structure, fulfill space separation condition and also due to computational efficiency [91, 119].

Renard and Marmonier [101] were the firsts to use a finite element discretization to model heterogeneous materials with a homogenization method. The geometry of the RVE is meshed with finite elements to solve the micro-scale Boundary Value Problem (BVP), then through homogenization rules the micro-results are linked to macro-scale properties [34, 35, 63, 107, 120]. Guedes and Kikuchi [36] extended the method to analyze the mechanical behavior of linear elastic 2D and 3D composite materials with periodic microstructure. However, who introduced the general formulation of FE2 was Feyel [22]. The structure at the macro-scale is discretized by finite elements and for each integration points of the macro-element one RVE also discretized by finite elements is assigned. The coupled problem between both scale are computationally performed by solving separate BVPs through the finite element method. During subsequent years, the FE2 computational technique has been further developed in the works of many authors [59, 69, 74, 75, 78, 105, 108, 123].

The recent reviews of Kanouté et al. [54], Geers et al. [30], McDowell [70] and Nguyen et al. [83] show that the computational multiscale methods have a clear potential to encourage important advances in modelling material non-linear behaviour e.g. viscoelasticity, plasticity, material fracture and among others. Because in general, the non-linear processes are the result of many complex mechanisms at the micro-scale level which depend of the specific analyzed material. Since the pioneering works of Swan [114], Smit et al. [108], Michel et al. [72], Miehe et al. [73] and Nemat-Nasser [81] many developments have been done on this issue for several authors [16, 24, 25, 48, 57, 59, 89, 115, 121].

One of the main challenges for computational multiscale formulations is the objectivity i.e. energy consistency and mesh/RVE-size independence [3]. The dissipated energy by the failure mechanisms must be consistent through the scales and, unaffected by RVE size [33] and convergent with mesh refinement. To overcome the inherent non-objective of classical multiscale computational homogenization due to size-effect associated with strain localization at the micro-scale several techniques have been developed. For instance, the Multiscale Aggregating Discontinuities (MAD) was proposed by Belytschko et al. [4], the strategy is based on aggregating discontinuities at the micro-scale and passing these to the macro-scale [5, 111]. In [86], the Continuum Strong Discontinuity Approach (CSDA) proposed by Oliver and Huespe [85, 87, 88] is extended to two-scale modeling of propagating fracture. In general, these strategies introduced in the formulation a characteristic length as a numerical parameter which is coming from the RVE domain size e.g. the finite element size [93], the bandwidth of crack [124] or the bandwidth of cohesive zone [86]. In addition, computational homogenization schemes using a gradient-enhanced to connect the scales

were developed [50, 60, 61, 65, 66, 112], in these kind of approaches it is not necessary to introduce artificially a length-scale parameter because it arrives naturally. Coenen et al. developed an enhanced multi-scale scheme by introducing discontinuities to simulate the strain localization band [14]. The same authors propose a new type of boundary condition at the micro-scale to improve capture the developing localization bands [13].

It is known that computational multiscale homogenization techniques are computationally expensive for non-linear analysis because the micro-scale problem needs to be solved many times. However, the multiscale homogenization solution is easily parallelizable due to the fact that the different micro-scale BVPs are independent of each other [23, 69, 80]. In addition, several recent contributions have been presented aiming at improving the robustness and reducing the computational cost e.g. adaptive strategies to solve the micro-scale problem only the minimum number of times necessary [93, 124], adaptive sub-incremental strategies to ensure the convergence of the multiscale solution in the presence of several sources of non-linearity [100, 110], model-order reduction techniques [41, 64, 79, 129] which use the Proper Orthogonal Decomposition (POD), or proper generalized decomposition, to obtain the reduced set of empirical shape functions.

In the last years, multiphysics problems have been addressed using multiscale homogenization methods, such as [8, 95, 118, 122] for thermomechanical problems, [11, 49] for magnetomechanical problems, [56, 77, 104] for electromechanical problems, among others. On the other hand, after the groundbreaking contribution of Bendsoe and Kikuchi [6] in which the homogenization method is used to design optimal topology structures several authors have dabbled into this actual research topic [1, 21, 55, 106, 128].

1.2 Formulation Introduction

In the context of solid mechanics and multiscale computational homogenization, one of the most extended and popular method is called First-Order Computational Homogenization (FOCH) [72, 74, 120]. In this approach, the macro-scale strain tensor (or deformation gradient tensor) is used as input to solve the micro-scale BVP. The material stress-strain relationship is obtained from the solution of problem at the micro-scale i.e. the RVE which contains the detailed modeling of the internal heterogeneous structure of the composite. Therefore, it does not require any composite constitutive assumption or compatibility equation to address the composite response [94]. And, there are not restriction on the constitutive model used in the component materials, even non-linear materials

and time-dependency models can be taken into account [89, 93, 108].

In the last decade, a Second-Order Computational Homogenization (SOCH) was proposed as a natural extension of the FOCH [50, 60, 61]. It was developed to be applied in critical regions of large gradient deformation, where the characteristic wave length of the macro-scale deformation field is of the order of the size of the micro-scale. In this method the macroscopic gradient of the deformation gradient is also incorporated as input in the micro-scale BVP. The first-order equilibrium problem is conserved at the micro-scale level, while a higher-order equilibrium problem appears at the structural scale. The finite element framework necessary for the numerical solution of the macro-scale problem leads to many complications [58], which has restricted its extensive applicability.

The SOCH is able to capture the second-order effects in the microscopic scale due to macroscopic high-order phenomena such as bending or strain localization, this is its major improvement over the FOCH. However, the FOCH conserves first-order equilibrium equations at both scales, which represents an advantage from a computational point of view. With the purpose to take the best of these two methods, the presented work proposes an Enhanced-First-Order Computational Homogenization (EFOCH). The developed procedure takes into account macroscopic second-order effects by using the macro-scale second-order deformation measure in the micro-scale BVP. Besides, the proposed EFOCH conserves the classical first-order equilibrium problem in the structural scale.

In the following, the classical FOCH is reviewed, as it is the most common procedure used in mechanical multiscale analysis. The description of the FOCH theory will be used to set the theoretical framework of homogenization procedures. Afterwards, Sect. 3 presents the proposed EFOCH, together with some remarks regarding the differences found with the SOCH proposed and used by other authors. In Sect. 4 the BVPs for both scales and some considerations about the numerical implementation are described. Section 5 contains the numerical examples used to compare the results obtained with the proposed EFOCH and FOCH. Finally in last section the conclusions of this work are exposed.

2 General Considerations and FOCH

The no lineal transformation between the reference configuration of the body Ω and the current configuration of the same body Ω^c is defined as: $\phi : \Omega \rightarrow \Omega^c \mid \mathbf{x} = \phi(\mathbf{X})$, where $\mathbf{x} \in \Omega^c$ and $\mathbf{X} \in \Omega$ are respectively the current and

the reference positions of the material point. Therefore, the linear mapping for an infinitesimal material line element is

$$d\mathbf{x} = \mathbf{F} \cdot d\mathbf{X}, \tag{1}$$

where the deformation gradient tensor is defined by

$$\mathbf{F} = \frac{\partial \phi}{\partial \mathbf{X}} = \nabla \mathbf{x}. \tag{2}$$

Here, the gradient operator $\nabla(\cdot)$ is taken respect to the reference configuration $\mathbf{X}$.

Nevertheless, if now a finite material line within a finite volume is considered, the expression given by (1) does not apply any more. However, a Taylor series expansion (centered at $\mathbf{X}_o$) can be used to obtain an expression for the finite material line $\Delta\mathbf{x}$ in the current configuration as

$$\Delta\mathbf{x} = \mathbf{F}(\mathbf{X}_o) \cdot \Delta\mathbf{X} + \frac{1}{2}\mathbf{G}(\mathbf{X}_o) : \Delta\mathbf{X} \otimes \Delta\mathbf{X} + \mathcal{O}(\Delta\mathbf{X}_o^3), \tag{3}$$

where the third-order tensor $\mathbf{G}$ is the gradient of the deformation gradient, which can be defined as

$$\mathbf{G} = \frac{\partial}{\partial \mathbf{X}}\left(\frac{\partial \phi}{\partial \mathbf{X}}\right) = \nabla \mathbf{F}. \tag{4}$$

It can be shown from (4) that the tensor $\mathbf{G}$ has the symmetry property of $G_{ijk} = G_{ikj}$ [60].

2.1 First-Order Computational Homogenization

Let us consider a solid domain (or body Ω) with a periodic or quasi-periodic microstructure that can be represented by a RVE. In this body, it is possible to establish two scale levels, a macro scale (or structural scale) for the macrostructure, and a micro scale (or sub scale) for the microstructure. The microstructural scale is defined using a RVE which characterizes the microstructure of the material. Let us also consider an infinitesimal material point $\mathbf{X}_o$ in the reference configuration of the structure, and the RVE around this considered point as Fig. 1 is showing.

The called principle of separation of scales [30] establishes that: the microstructural length scale l_μ is assumed to be much smaller than the macrostructural characteristic length l, which is the length over the macroscopic space. In other words, the principle says that the existing periodical microscopic dimension around of the macrostructural point ($\mathbf{X}_o$) must be smaller than the characteristic macrostructural dimension. If this principle is satisfied, the current configuration or deformed position of a material point in the RVE $\mathbf{x}_\mu \in \Omega_\mu^c$ can be approximated as

$$\mathbf{x}_\mu(\mathbf{X}_o, \mathbf{X}_\mu) \cong \mathbf{x}_\mu^o + \mathbf{F}(\mathbf{X}_o) \cdot \Delta\mathbf{X}_\mu + \mathbf{w}(\mathbf{X}_\mu), \tag{5}$$

where $\Delta\mathbf{X}_\mu = \mathbf{X}_\mu - \mathbf{X}_\mu^o$, and $\mathbf{X}_\mu \in \Omega_\mu$ is the reference configuration or non-deformed position of the material
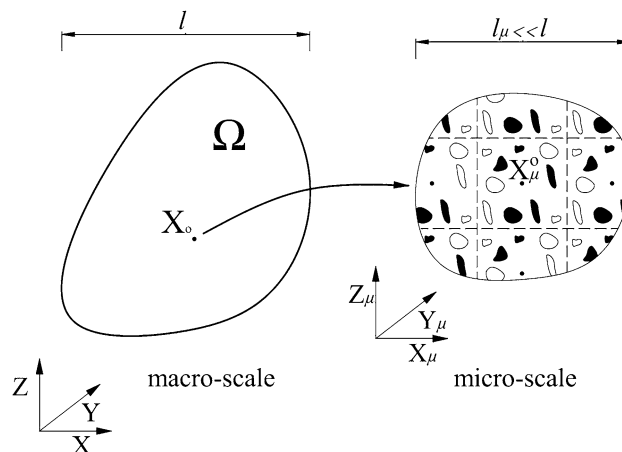

Fig. 1 Macrostructure and microstructure around of the point $\mathbf{X}_o$

point in the RVE and $\mathbf{X}_\mu^o$ and $\mathbf{x}_\mu^o$ are the origin of the reference and the current coordinate system on the RVE, respectively (see Fig. 2). The extra term $\mathbf{w}$ is a microstructural displacement fluctuation field.

To simplify the symbolic manipulation of the formulation is convenient to set the coordinate system's origin as

$$\mathbf{X}_\mu^o = 0 \qquad \text{and} \qquad \mathbf{x}_\mu^o = 0. \tag{6}$$

Later, it will be proved that with these values, the rigid body motion of the RVE is avoided. Considering these restrictions, the expression given by (5) can be rewritten as

$$\mathbf{x}_\mu(\mathbf{X}_o, \mathbf{X}_\mu) \cong \mathbf{F}(\mathbf{X}_o) \cdot \mathbf{X}_\mu + \mathbf{w}(\mathbf{X}_\mu). \tag{7}$$

2.1.1 Displacement Field on the RVE

The displacement field $\mathbf{u}_\mu$ at the RVE is defined by

$$\mathbf{u}_\mu = \mathbf{x}_\mu - \mathbf{X}_\mu, \tag{8}$$

and taking into account (7) in the previous equation,

$$\mathbf{u}_\mu(\mathbf{X}_o, \mathbf{X}_\mu) \cong [\mathbf{F}(\mathbf{X}_o) - \mathbf{I}] \cdot \mathbf{X}_\mu + \mathbf{w}(\mathbf{X}_\mu), \tag{9}$$

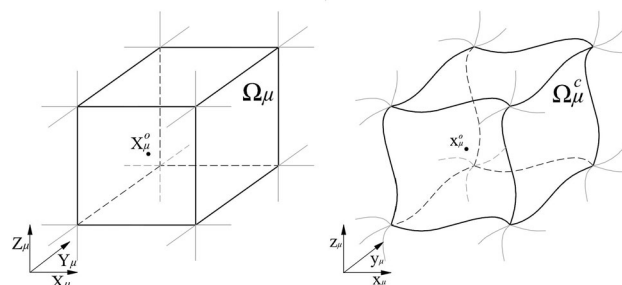where $\mathbf{I}$ is the second-order unit tensor.

Fig. 2 Reference and current configuration of the RVE

2.1.2 Kinematically Admissible Displacement Fields and Boundary Conditions

The displacement fields in the RVE that are kinematically admissible are obtained as a result of the coupling between the macrostructure and the microstructure. This linkage is based on the average theorems and they have been initially proposed for infinitesimal deformations by Hill [42]. Later, Hill [46] and Nemat-Nasser [82] extended these to finite deformations.

The first of the averaging relations postulates that the volume average of the microstructural deformation gradient tensor $\mathbf{F}_\mu$ over the RVE must be equal to the macroscopic $\mathbf{F}$. In the considered point $\mathbf{X}_o$ this is

$$\mathbf{F}(\mathbf{X}_o) = \frac{1}{V_\mu} \int_{\Omega_\mu} \mathbf{F}_\mu(\mathbf{X}_o, \mathbf{X}_\mu)\, dV, \tag{10}$$

where V_μ is the volume of the RVE in the reference configuration.

Considering (7) it is possible to write $\mathbf{F}_\mu$ as

$$\begin{aligned}\mathbf{F}_\mu(\mathbf{X}_o, \mathbf{X}_\mu) &= \nabla \mathbf{x}_\mu(\mathbf{X}_o, \mathbf{X}_\mu) \\ &\cong \mathbf{F}(\mathbf{X}_o) + \nabla \mathbf{w}(\mathbf{X}_\mu),\end{aligned} \tag{11}$$

and using this relation, the right hand size of (10) is

$$\begin{aligned}\frac{1}{V_\mu} \int_{\Omega_\mu} \mathbf{F}_\mu(\mathbf{X}_o, \mathbf{X}_\mu)\, dV &= \frac{1}{V_\mu} \int_{\Omega_\mu} \nabla \mathbf{x}_\mu(\mathbf{X}_o, \mathbf{X}_\mu)\, dV \\ &= \mathbf{F}(\mathbf{X}_o) + \frac{1}{V_\mu} \int_{\Omega_\mu} \nabla \mathbf{w}(\mathbf{X}_\mu)\, dV.\end{aligned} \tag{12}$$

Equation (12) can be rewritten as

$$\begin{aligned}\mathbf{F}(\mathbf{X}_o) = &\frac{1}{V_\mu} \int_{\Omega_\mu} \mathbf{F}_\mu(\mathbf{X}_o, \mathbf{X}_\mu)\, dV \\ &- \frac{1}{V_\mu} \int_{\Omega_\mu} \nabla \mathbf{w}(\mathbf{X}_\mu)\, dV,\end{aligned} \tag{13}$$

or

$$\begin{aligned}\mathbf{F}(\mathbf{X}_o) = &\frac{1}{V_\mu} \int_{\Omega_\mu} \nabla \mathbf{x}_\mu(\mathbf{X}_o, \mathbf{X}_\mu)\, dV \\ &- \frac{1}{V_\mu} \int_{\Omega_\mu} \nabla \mathbf{w}(\mathbf{X}_\mu)\, dV.\end{aligned} \tag{14}$$

Finally, applying the divergence theorem, in the right hand size of (14), this can be also rewritten in term of surface integral as

$$\begin{aligned}\mathbf{F}(\mathbf{X}_o) = &\frac{1}{V_\mu} \int_{\partial\Omega_\mu} \mathbf{x}_\mu(\mathbf{X}_o, \mathbf{X}_\mu) \otimes \mathbf{N}\, dA \\ &- \frac{1}{V_\mu} \int_{\partial\Omega_\mu} \mathbf{w}(\mathbf{X}_\mu) \otimes \mathbf{N}\, dA,\end{aligned} \tag{15}$$

where $\partial\Omega_\mu$ is the RVE boundary domain in the reference configuration, and $\mathbf{N}$ denotes the outward unit normal on $\partial\Omega_\mu$.

Clearly, to satisfy the first average theorem, the integrals that depend of the displacement fluctuation in both (14) and (15) must vanish. Therefore,

$$\int_{\Omega_\mu} \nabla \mathbf{w}(\mathbf{X}_\mu)\, dV = \mathbf{0} \tag{16}$$

and

$$\int_{\partial\Omega_\mu} \mathbf{w}(\mathbf{X}_\mu) \otimes \mathbf{N}\, dA = \mathbf{0}. \tag{17}$$

Noting Fig. 2 and considering that the reference geometry configuration of the RVE is originally a cube, as the figure is showing, the integral restriction on the RVE boundary can be splitted in the different surfaces of the $\partial\Omega_\mu$ domain. Besides, taking the reference coordinate system that is shown in Fig. 3, the outward unit normal of the cubic faces satisfy: $\mathbf{N}_X^- = -\mathbf{N}_X^+$, $\mathbf{N}_Y^- = -\mathbf{N}_Y^+$ and $\mathbf{N}_Z^- = -\mathbf{N}_Z^+$. Here, the subscript makes reference to the axis which is perpendicular to the considered face and the superscript defines the position of the face on the axis. Therefore, considering this geometry, the expression given by (17) may be rewritten as

$$\sum_{i=X,Y,Z} \left(\int_{\mathbf{N}_i^+} \mathbf{w}\, dA - \int_{\mathbf{N}_i^-} \mathbf{w}\, dA \right) \otimes \mathbf{N}_i^+ = \mathbf{0} \tag{18}$$

Equation (18) shows that the boundary restriction on the displacement fluctuation field can be splitted on the different surface pairs (X, Y and Z) of the RVE boundary.
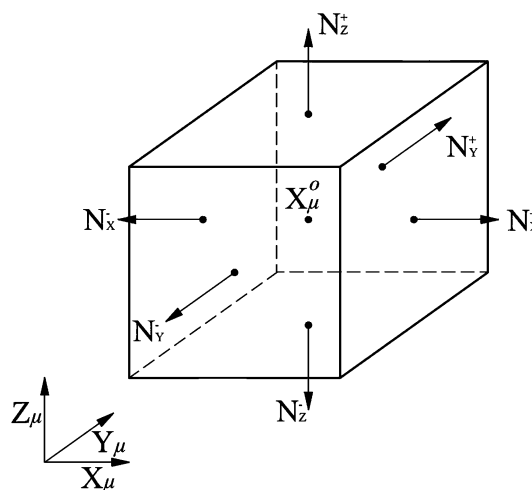

Fig. 3 Normal vectors to the surfaces in the reference configuration of a Cubic RVE

Previous equations from (16) to (18) can be used to obtain the different displacement fluctuation fields kinematically admissible in the microstructural level. Several models have been defined that assume different fluctuation fields:

1. *Taylor model* (or zero fluctuations): The expression given by (16) is verified when

   $$\mathbf{w}, \text{ sufficiently regular} \mid \mathbf{w}(\mathbf{X}_\mu) = \mathbf{0}, \quad \forall \mathbf{X}_\mu \in \Omega_\mu. \tag{19}$$

   This model gives homogeneous deformation in the microstructural scale level (see 24).

2. *Linear boundary displacements* (or zero boundary fluctuations): The expression given by (17) is verified when

   $$\mathbf{w}, \text{ sufficiently regular} \mid \mathbf{w}(\mathbf{X}_\mu) = \mathbf{0}, \quad \forall \mathbf{X}_\mu \in \partial\Omega_\mu. \tag{20}$$

   The deformation of the RVE boundary domain for this class are fully prescribed.

3. *Periodic boundary fluctuations*: The key kinematical constraint for this class is that $\mathbf{w}$ must be periodic on the different faces of the RVE. That is, for each pair $\left\{\mathbf{X}_\mu^+, \mathbf{X}_\mu^-\right\}$ of boundary points the expression given by (18) is verified when

   $$\mathbf{w}, \text{ suff. reg.} \mid \mathbf{w}\left(\mathbf{X}_\mu^+\right) = \mathbf{w}\left(\mathbf{X}_\mu^-\right),$$
   $$\forall \text{ pairs } \left\{\mathbf{X}_\mu^+, \mathbf{X}_\mu^-\right\} \in \partial\Omega_\mu. \tag{21}$$

4. *Minimal constraint* (or uniform boundary traction): In this constraint the nontrivial solution of (17) is obtained.

2.1.3 Microscopic and Macroscopic Strain Tensor

Considering a infinitesimal deformation framework the strain tensor in the microstructural level can be obtained as

$$\begin{aligned}
\mathbf{E}_\mu(\mathbf{X}_o, \mathbf{X}_\mu) &= \frac{1}{2}\left(\mathbf{F}_\mu(\mathbf{X}_o, \mathbf{X}_\mu) + \mathbf{F}_\mu^T(\mathbf{X}_o, \mathbf{X}_\mu)\right) - \mathbf{I} \\
&= \frac{1}{2}\left(\mathbf{F}(\mathbf{X}_o) + \mathbf{F}^T(\mathbf{X}_o)\right) - \mathbf{I} \\
&\quad + \frac{1}{2}\left(\nabla\mathbf{w}(\mathbf{X}_\mu) + (\nabla\mathbf{w}(\mathbf{X}_\mu))^T\right),
\end{aligned} \tag{22}$$

and, if (10) is satisfied it can be proved that taking the volume average of $\mathbf{E}_\mu$ over the RVE domain the following relationship is obtained,

$$\begin{aligned}
&\frac{1}{V_\mu} \int_{\Omega_\mu} \mathbf{E}_\mu(\mathbf{X}_o, \mathbf{X}_\mu) \, dV \\
&\quad = \frac{1}{2}\left(\mathbf{F}(\mathbf{X}_o) + \mathbf{F}^T(\mathbf{X}_o)\right) - \mathbf{I} = \mathbf{E}(\mathbf{X}_o).
\end{aligned} \tag{23}$$

Here, $\mathbf{E}(\mathbf{X}_o)$ is the macroscopic strain tensor. It is possible to rewrite (22) as

$$\mathbf{E}_\mu(\mathbf{X}_o, \mathbf{X}_\mu) = \mathbf{E}(\mathbf{X}_o) + \mathbf{E}_\mu^w(\mathbf{X}_\mu), \tag{24}$$

where $\mathbf{E}_\mu^w = \frac{1}{2}\left(\nabla\mathbf{w} + (\nabla\mathbf{w})^T\right) = \nabla^s\mathbf{w}$ is the contribution of $\mathbf{w}$ to the microscopic strain tensor and ∇^s is the symmetric gradient operator. Because (10) is verified the volume average of $\mathbf{E}_\mu^w$ over the RVE domain is equal to zero.

2.1.4 Hill–Mandel Principle and RVE Equilibrium

The Hill–Mandel energy condition [43, 68], also referred to as the macro-homogeneity condition, states that the virtual work of the point $\mathbf{X}_o$ considered must be equal to the volume average of the virtual work in the RVE to any kinematically admissible displacement field, this principle can be formulated as

$$\mathbf{S} : \delta\mathbf{E}(\mathbf{X}_o) = \frac{1}{V_\mu} \int_{\Omega_\mu} \mathbf{S}_\mu : \delta\mathbf{E}_\mu \, dV, \tag{25}$$

where $\mathbf{S}$ and $\mathbf{S}_\mu$ are the macroscopic and microscopic stress tensor, respectively.

Using (24), the principle is rewritten as

$$\begin{aligned}
\mathbf{S} : \delta\mathbf{E}(\mathbf{X}_o) &= \frac{1}{V_\mu} \int_{\Omega_\mu} \mathbf{S}_\mu \, dV : \delta\mathbf{E}(\mathbf{X}_o) \\
&\quad + \frac{1}{V_\mu} \int_{\Omega_\mu} \mathbf{S}_\mu : \delta\mathbf{E}_\mu^w(\mathbf{X}_\mu) \, dV.
\end{aligned} \tag{26}$$

Taking $\mathbf{S}$ as the volume average of $\mathbf{S}_\mu$ in the RVE domain, which is similar to the first average relation (see 10)

$$\mathbf{S}(\mathbf{X}_o, \mathbf{X}_\mu) \equiv \frac{1}{V_\mu} \int_{\Omega_\mu} \mathbf{S}_\mu(\mathbf{X}_o, \mathbf{X}_\mu) \, dV, \tag{27}$$

Eq. (26) will be satisfied if

$$\int_{\Omega_\mu} \mathbf{S}_\mu : \delta\mathbf{E}_\mu^w(\mathbf{X}_\mu) \, dV = \int_{\Omega_\mu} \mathbf{S}_\mu : \nabla^s\delta\mathbf{w} \, dV = 0. \tag{28}$$

Therefore, the RVE's variational equilibrium equation is

$$\int_{\Omega_\mu} \mathbf{S}_\mu : \nabla^s\delta\mathbf{w} \, dV = 0, \tag{29}$$

which must be satisfied for any kinematically admissible $\mathbf{w}$ (see Sect. 2.1.2).

It is possible to observe that because of the symmetry of $\mathbf{S}_\mu$ it can be proved that $\mathbf{S}_\mu : (\nabla\mathbf{a}) = \mathbf{S}_\mu : (\nabla\mathbf{a})^T$, where $\mathbf{a}$ is a first-order tensor, Eq. (28) also can be rewritten as

$$\int_{\Omega_\mu} \mathbf{S}_\mu : \delta\mathbf{E}_\mu^w(\mathbf{X}_\mu) \, dV = \int_{\Omega_\mu} \mathbf{S}_\mu : \nabla\delta\mathbf{w} \, dV = 0. \tag{30}$$

2.1.5 Microscopic and Macroscopic Stress Tensor

The microscopic stress tensor can be obtained as

$$
\begin{aligned}
\mathbf{S}_\mu(\mathbf{X}_o, \mathbf{X}_\mu) &= \mathbf{C}_\mu(\mathbf{X}_\mu) : \mathbf{E}_\mu(\mathbf{X}_o, \mathbf{X}_\mu) \\
&= \mathbf{C}_\mu(\mathbf{X}_\mu) : \mathbf{E}(\mathbf{X}_o) + \mathbf{C}_\mu(\mathbf{X}_\mu) : \mathbf{E}_\mu^w(\mathbf{X}_\mu),
\end{aligned}
\tag{31}
$$

where $\mathbf{C}_\mu$ is the material constitutive tensor in the RVE. Then, using (27) the macroscopic stress tensor is

$$
\begin{aligned}
\mathbf{S}(\mathbf{X}_o, \mathbf{X}_\mu) &= \bar{\mathbf{C}} : \mathbf{E}(\mathbf{X}_o) \\
&+ \frac{1}{V_\mu} \int_{\Omega_\mu} \mathbf{C}_\mu : \mathbf{E}_\mu^w(\mathbf{X}_\mu)\, dV,
\end{aligned}
\tag{32}
$$

where,

$$
\bar{\mathbf{C}} \equiv \frac{1}{V_\mu} \int_{\Omega_\mu} \mathbf{C}_\mu \, dV
\tag{33}
$$

is a constitutive tensor, which can be considered a material property.

Equation (32) shows that $\mathbf{S}$ depends of $\mathbf{E}$ and also of $\mathbf{E}_\mu^w$. Moreover, $\mathbf{X}_\mu$ does not appear explicitly in $\mathbf{E}_\mu^w$ expression (see 24) and, consequently, $\mathbf{X}_\mu$ does not appear in $\mathbf{S}_\mu$ either. This implies that, the periodic microstructure around the macro point $\mathbf{X}_o$ does not have to be modeled with its exact dimensions. A non-dimensional RVE with the internal distribution and volume fractions of the simple materials is enough to obtain the microscopic strain and stress fields.

On the other hand, the kinematically admissible displacement fluctuation option used to satisfy the boundary condition affects the final $\mathbf{S}$ obtained, as occurs in the Taylor model case. This means that if there is a null displacement fluctuation field in the total RVE domain, the $\mathbf{S}$ obtained only depend of $\mathbf{E}$ and $\bar{\mathbf{C}}$. In other words, the Taylor model condition returns the classical mixing theory results.

3 Enhanced-First-Order Computational Homogenization

In the following, an Enhanced-First-Order Computational Homogenization (EFOCH) is proposed with the main objective to include in the RVE the second-order effects obtained from a macroscopic high-order phenomena. Unlike the SOCH, the presented EFOCH preserves a classical first-order BVP at the macro scale level as does the FOCH.

If the principle of separation of scales is not clearly satisfied, the microscopic displacement field can be enriched with second-order information available in the macro scale. The deformed position of a material point in the

RVE (see 5), can be rewritten with the second-order term of (3). Then, it is possible to propose a new approximation of the current configuration as

$$
\begin{aligned}
\mathbf{x}_\mu(\mathbf{X}_o, \mathbf{X}_\mu) &\cong \mathbf{x}_\mu^c + \mathbf{F}(\mathbf{X}_o) \cdot \Delta \mathbf{X}_\mu \\
&+ \frac{1}{2} \mathbf{G}(\mathbf{X}_o) : \Delta \mathbf{X}_\mu \otimes \Delta \mathbf{X}_\mu + \mathbf{w}(\mathbf{X}_\mu),
\end{aligned}
\tag{34}
$$

and setting the coordinate system's origin as defined in (6), the proposed deformed position of the RVE is

$$
\begin{aligned}
\mathbf{x}_\mu(\mathbf{X}_o, \mathbf{X}_\mu) &\cong \mathbf{F}(\mathbf{X}_o) \cdot p\mathbf{X}_\mu \\
&+ \frac{1}{2} \mathbf{G}(\mathbf{X}_o) : \mathbf{X}_\mu \otimes \mathbf{X}_\mu + \mathbf{w}(\mathbf{X}_\mu).
\end{aligned}
\tag{35}
$$

And the proposed displacement field $\mathbf{u}_\mu$ on the RVE (see 8) can be obtained now as

$$
\begin{aligned}
\mathbf{u}_\mu(\mathbf{X}_o, \mathbf{X}_\mu) &\cong [\mathbf{F}(\mathbf{X}_o) - \mathbf{I}] \cdot p\mathbf{X}_\mu \\
&+ \frac{1}{2} \mathbf{G}(\mathbf{X}_o) : \mathbf{X}_\mu \otimes \mathbf{X}_\mu + \mathbf{w}(\mathbf{X}_\mu).
\end{aligned}
\tag{36}
$$

Noting that an extra term appears by including $\mathbf{G}$ in (34). This extra second-order term is a new linking term between the macroscopic and microscopic scales.

3.1 Kinematically Admissible Displacement Fields and Boundary Conditions

The first of the average postulates (see 10) is used again to obtain the admissible displacement fields. The microscopic deformation gradient considering the expression given by (35) is

$$
\begin{aligned}
\mathbf{F}_\mu(\mathbf{X}_o, \mathbf{X}_\mu) &= \nabla \mathbf{x}_\mu(\mathbf{X}_o, \mathbf{X}_\mu) \\
&\cong \mathbf{F}(\mathbf{X}_o) + \mathbf{G}(\mathbf{X}_o) \cdot \mathbf{X}_\mu + \nabla \mathbf{w}(\mathbf{X}_\mu).
\end{aligned}
\tag{37}
$$

And, the volume average of $\mathbf{F}_\mu$ over the RVE is

$$
\begin{aligned}
\frac{1}{V_\mu} \int_{\Omega_\mu} \mathbf{F}_\mu(\mathbf{X}_o, \mathbf{X}_\mu)\, dV &= \frac{1}{V_\mu} \int_{\Omega_\mu} \nabla \mathbf{x}_\mu(\mathbf{X}_o, \mathbf{X}_\mu)\, dV \\
&= \mathbf{F}(\mathbf{X}_o) + \mathbf{G}(\mathbf{X}_o) \cdot \frac{1}{V_\mu} \int_{\Omega_\mu} \mathbf{X}_\mu \, dV \\
&+ \frac{1}{V_\mu} \int_{\Omega_\mu} \nabla \mathbf{w}(\mathbf{X}_\mu)\, dV.
\end{aligned}
\tag{38}
$$

It can be proved that if the RVE geometry in the reference configuration is originally a cube, as shown in Fig. 2, and the position of the origin of the coordinate system is defined at the center of the RVE, then the first moment of volume of the RVE is

$$
\int_{\Omega_\mu} \mathbf{X}_\mu \, dV = \mathbf{0}.
\tag{39}
$$

Therefore, (38) can be rewritten as (13) or (14), and the restrictions on $\mathbf{w}$ are the same than the one obtained for the FOCH, which are shown in (16)–(18). The fields

kinematically admissible **w** presented in Sect. 2.1.2 are still valid for the proposed EFOCH.

3.1.1 Extra Kinematic Restrictions and Boundary Conditions

The next step consists in obtaining the kinematic restrictions result of including the new term **G** in $\mathbf{u}_\mu$. In other words, some extension of the first average theorem needs to be proposed in term of **G**. In the following, a natural extension for the first average theorem is presented. The main drawback of this proposal is that leads to restrictions on the derivative displacement fluctuation field and therefore, a high-order problem on the RVE must be considered. To avoid this situation, and in order to continue using the classical first-order BVP on the RVE, the alternative extension proposed by Kouznetsova [60] is also shown.

Natural extension of the first average theorem
The first natural possibility for this extension could be

$$\mathbf{G}(\mathbf{X}_o) = \frac{1}{V_\mu} \int_{\Omega_\mu} \mathbf{G}_\mu(\mathbf{X}_o, \mathbf{X}_\mu) \, dV. \tag{40}$$

Note that (40) is similar to (10) but in this case, the volume average of $\mathbf{G}_\mu$ over the RVE must be equal to **G** in the considered point $\mathbf{X}_o$.

Considering (37) and (4), $\mathbf{G}_\mu$ can be written as

$$\begin{aligned}\mathbf{G}_\mu(\mathbf{X}_o, \mathbf{X}_\mu) &= \nabla(\nabla \mathbf{x}_\mu(\mathbf{X}_o, \mathbf{X}_\mu)) \\ &\cong \mathbf{G}(\mathbf{X}_o) + \nabla(\nabla \mathbf{w}(\mathbf{X}_\mu)).\end{aligned} \tag{41}$$

Using (41) and taking the volume average over the RVE it is possible to obtain

$$\begin{aligned}\mathbf{G}(\mathbf{X}_o) =\,& \frac{1}{V_\mu} \int_{\Omega_\mu} \mathbf{G}_\mu(\mathbf{X}_o, \mathbf{X}_\mu) \, dV \\ &- \frac{1}{V_\mu} \int_{\Omega_\mu} \nabla(\nabla \mathbf{w}(\mathbf{X}_\mu)) \, dV,\end{aligned} \tag{42}$$

or

$$\begin{aligned}\mathbf{G}(\mathbf{X}_o) =\,& \frac{1}{V_\mu} \int_{\Omega_\mu} \nabla(\nabla \mathbf{x}_\mu(\mathbf{X}_o, \mathbf{X}_\mu)) \, dV \\ &- \frac{1}{V_\mu} \int_{\Omega_\mu} \nabla(\nabla \mathbf{w}(\mathbf{X}_\mu)) \, dV.\end{aligned} \tag{43}$$

And, applying the divergence theorem in the last expression

$$\begin{aligned}\mathbf{G}(\mathbf{X}_o) =\,& \frac{1}{V_\mu} \int_{\partial\Omega_\mu} \nabla \mathbf{x}_\mu(\mathbf{X}_o, \mathbf{X}_\mu) \otimes \mathbf{N} \, dA \\ &- \frac{1}{V_\mu} \int_{\partial\Omega_\mu} \nabla \mathbf{w}(\mathbf{X}_\mu) \otimes \mathbf{N} \, dA.\end{aligned} \tag{44}$$

Similarly as in FOCH, to satisfy the proposed extension of the first average theorem, the integrals that depend of the displacement fluctuation in (42) and (44) must vanish, then

$$\int_{\Omega_\mu} \nabla(\nabla \mathbf{w}(\mathbf{X}_\mu)) \, dV = \mathbf{0}, \tag{45}$$

and

$$\int_{\partial\Omega_\mu} \nabla \mathbf{w}(\mathbf{X}_\mu) \otimes \mathbf{N} \, dA = \mathbf{0}. \tag{46}$$

The last expression represents an extra integral restriction on the derivative displacement fluctuation field. Taking the same consideration than before regarding the geometry of the RVE (see Fig. 3), the boundary integration in (46) can be splitted in

$$\sum_{i=X,Y,Z} \left(\int_{\mathbf{N}_i^+} \nabla \mathbf{w} \, dA - \int_{\mathbf{N}_i^-} \nabla \mathbf{w} \, dA \right) \otimes \mathbf{N}_i^+ = \mathbf{0}. \tag{47}$$

Some components of the integrals can also be rewritten in terms of line-boundary integrals applying the divergence theorem. For example, if the first left integral in the first term in (47) is taken, the line-boundary of this surface integral can be separated in four different lines, two perpendiculars to Y axis, and the other two perpendiculars to Z axis, as it is shown in Fig. 4. Because of the RVE geometry considered, these lines boundary have the property of $\mathbf{N}_{X|Y}^- = -\mathbf{N}_{X|Y}^+$ and $\mathbf{N}_{X|Z}^- = -\mathbf{N}_{X|Z}^+$. Then, with this information the considered integral can be rewritten as

$$\begin{aligned}\int_{\mathbf{N}_X^+} \nabla \mathbf{w} \, dA_{yz} =\,& \int_{\mathbf{N}_X^+} \nabla_X \mathbf{w} \, dA_{yz} \\ &+ \left(\int_{\mathbf{N}_{X|Y}^+} \mathbf{w} \, dL_z - \int_{\mathbf{N}_{X|Y}^-} \mathbf{w} \, dL_z \right) \otimes \mathbf{N}_{X|Y}^+ \\ &+ \left(\int_{\mathbf{N}_{X|Z}^+} \mathbf{w} \, dL_y - \int_{\mathbf{N}_{X|Z}^-} \mathbf{w} \, dL_y \right) \otimes \mathbf{N}_{X|Z}^+,\end{aligned} \tag{48}$$

where ∇_X represents the derivative with respect to the X axis. This term cannot be reduced to a line-integral using
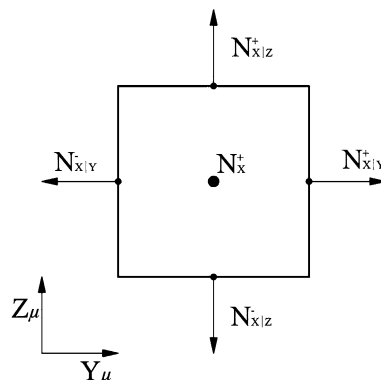

Fig. 4 Normal vectors to the projection lines in the YZ surface of the Cubic RVE

the divergence theorem. It can be seen that when the *Periodic boundary fluctuations* condition is the kinematically admissible option used for $\mathbf{w}$ on the RVE, the two right terms on (48) are satisfied directly. The points on the opposing lines are a pair boundary points that have the same displacement fluctuation because of the kinematic condition imposed. Applying this same procedure to the rest of the terms of expression (47), this equation can be rewritten as

$$\sum_{i=X,Y,Z} \left(\int_{\mathbf{N}_i^+} \nabla_i \mathbf{w}\, dA - \int_{\mathbf{N}_i^-} \nabla_i \mathbf{w} dA \right) \otimes \mathbf{N}_i^+ = \mathbf{0}. \qquad (49)$$

The previous expression represents an extra restriction on the displacement fluctuation field that makes it kinematically admissible in the RVE. A possible set of boundary conditions that satisfies this restriction is

$$\int_{\mathbf{N}_i^+} \nabla_i \mathbf{w}\, dA = \int_{\mathbf{N}_i^-} \nabla_i \mathbf{w}\, dA, \ \forall\, i = X, Y, Z \qquad (50)$$

Equation (49) is analogous to (18) but it is written in terms of derived displacement fluctuation field, in this case, on the normal direction of the pair surfaces (see Fig. 3). Therefore, to satisfy any kinematic restriction, as for example (50), obtained from (49), a high-order problem on the microscopic scale must be considered because the restriction of $\mathbf{w}$ is written on its derivate.

Alternative extension of the first average theorem

An alternative to the proposed extension of the averaging theorem given by (40) should be found in order to keep a classical BVP on the microstructural RVE problem. With this aim Kouznetsova [60] proposed another extension of the first average theorem. The proposed condition imposes that the second moment of area of the deformed RVE, given in terms of the microscopic displacements, must be equal to the second moment of area of the RVE expressed in terms of macroscopic deformation variables [50]. Considering the above, the expression given by (37) is multiplied by $\mathbf{X}_\mu$ and integrated over the RVE volume to obtain

$$\int_{\Omega_\mu} \nabla \mathbf{x}_\mu(\mathbf{X}_o, \mathbf{X}_\mu) \otimes \mathbf{X}_\mu\, dV = \mathbf{F}(\mathbf{X}_o) \otimes \int_{\Omega_\mu} \mathbf{X}_\mu\, dV$$
$$+ \mathbf{G}(\mathbf{X}_o) \cdot \int_{\Omega_\mu} \mathbf{X}_\mu \otimes \mathbf{X}_\mu\, dV$$
$$+ \int_{\Omega_\mu} \nabla \mathbf{w}(\mathbf{X}_\mu) \otimes \mathbf{X}_\mu\, dV. \qquad (51)$$

Knowing that the first moment of volume of the undeformed RVE is zero (see 39), and defining the second moment of volume of the undeformed RVE as $\mathbf{J} = \int_{\Omega_\mu} \mathbf{X}_\mu \otimes \mathbf{X}_\mu\, dV$. Equation (51) can be rewritten as

$$\mathbf{G}(\mathbf{X}_o) \cdot \mathbf{J} = \int_{\Omega_\mu} \nabla \mathbf{x}_\mu(\mathbf{X}_o, \mathbf{X}_\mu) \otimes \mathbf{X}_\mu\, dV$$
$$- \int_{\Omega_\mu} \nabla \mathbf{w}(\mathbf{X}_\mu) \otimes \mathbf{X}_\mu\, dV, \qquad (52)$$

replacing the following relationships

$$\nabla \mathbf{x}_\mu(\mathbf{X}_o, \mathbf{X}_\mu) \otimes \mathbf{X}_\mu = \nabla \big(\mathbf{x}_\mu(\mathbf{X}_o, \mathbf{X}_\mu) \otimes \mathbf{X}_\mu \big)$$
$$- \mathbf{x}_\mu(\mathbf{X}_o, \mathbf{X}_\mu) \otimes \mathbf{I}, \qquad (53)$$

and

$$\nabla \mathbf{w}(\mathbf{X}_\mu) \otimes \mathbf{X}_\mu = \nabla \big(\mathbf{w}(\mathbf{X}_\mu) \otimes \mathbf{X}_\mu \big) - \mathbf{w}(\mathbf{X}_\mu) \otimes \mathbf{I}, \qquad (54)$$

it is obtained

$$\mathbf{G}(\mathbf{X}_o) \cdot \mathbf{J} = \int_{\Omega_\mu} \nabla \big(\mathbf{x}_\mu(\mathbf{X}_o, \mathbf{X}_\mu) \otimes \mathbf{X}_\mu \big)\, dV$$
$$- \int_{\Omega_\mu} \nabla \big(\mathbf{w}(\mathbf{X}_\mu) \otimes \mathbf{X}_\mu \big)\, dV$$
$$- \int_{\Omega_\mu} \mathbf{x}_\mu(\mathbf{X}_o, \mathbf{X}_\mu)\, dV \otimes \mathbf{I}$$
$$+ \int_{\Omega_\mu} \mathbf{w}(\mathbf{X}_\mu) dV \otimes \mathbf{I}. \qquad (55)$$

Using (35) it can be shown that

$$\int_{\Omega_\mu} \mathbf{x}_\mu(\mathbf{X}_o, \mathbf{X}_\mu)\, dV \otimes \mathbf{I} = \frac{1}{2} \mathbf{G}(\mathbf{X}_o) : \mathbf{J} \otimes \mathbf{I}$$
$$+ \int_{\Omega_\mu} \mathbf{w}(\mathbf{X}_\mu)\, dV \otimes \mathbf{I}, \qquad (56)$$

which is used to obtain the final version of the sought expression

$$\mathbf{G}(\mathbf{X}_o) \cdot \mathbf{J} + \frac{1}{2} \mathbf{G}(\mathbf{X}_o) : \mathbf{J} \otimes \mathbf{I}$$
$$= \int_{\Omega_\mu} \nabla \big(\mathbf{x}_\mu(\mathbf{X}_o, \mathbf{X}_\mu) \otimes \mathbf{X}_\mu \big)\, dV \qquad (57)$$
$$- \int_{\Omega_\mu} \nabla \big(\mathbf{w}(\mathbf{X}_\mu) \otimes \mathbf{X}_\mu \big)\, dV,$$

Applying the divergence theorem on the right hand size of the equation, it can be rewritten in term of surface integral as

$$\mathbf{G}(\mathbf{X}_o) \cdot \mathbf{J} + \frac{1}{2} \mathbf{G}(\mathbf{X}_o) : \mathbf{J} \otimes \mathbf{I}$$
$$= \int_{\partial\Omega_\mu} \mathbf{x}_\mu(\mathbf{X}_o, \mathbf{X}_\mu) \otimes \mathbf{X}_\mu \otimes \mathbf{N}\, dA \qquad (58)$$
$$- \int_{\partial\Omega_\mu} \mathbf{w}(\mathbf{X}_\mu) \otimes \mathbf{X}_\mu \otimes \mathbf{N}\, dA.$$

It is possible to make a parallelism between (15) and (58). The additional condition regarding the second moment of

area of the deformed RVE given by (51) requires that the influence of **w** should vanish, then

$$\int_{\partial \Omega_\mu} \mathbf{w}(\mathbf{X}_\mu) \otimes \mathbf{X}_\mu \otimes \mathbf{N} \, dA = \mathbf{0}. \tag{59}$$

Equation (59) is a boundary restriction for **w**, then it is not necessary a high-order BVP, at microscopic scale, to satisfy the new boundary conditions deduced from it. Considering again the cubic geometry in the reference configuration defined previously for the RVE (see Fig. 3), the restriction given by (59) can be splitted in the different surfaces of the domain as

$$\sum_{i=X,Y,Z} \left(\int_{\mathbf{N}_i^+} \mathbf{w} \otimes \mathbf{X}_\mu \, dA - \int_{\mathbf{N}_i^-} \mathbf{w} \otimes \mathbf{X}_\mu \, dA \right) \otimes \mathbf{N}_i^+ = \mathbf{0}. \tag{60}$$

The last expression is used in Sect. 4.2 to obtain the BVP on the RVE for the EFOCH. In the case of *Periodic boundary fluctuations* condition, it can be proved that the expression (60) is automatically satisfied if

$$\int_{\mathbf{N}_X^-} \mathbf{w} \, dA_{yz} = \mathbf{0}, \quad \int_{\mathbf{N}_Y^-} \mathbf{w} \, dA_{xz} = \mathbf{0} \quad \text{and} \quad \int_{\mathbf{N}_Z^-} \mathbf{w} \, dA_{xy} = \mathbf{0}. \tag{61}$$

Therefore, the extra boundary condition required in this case is that the integral of the periodic displacement fluctuations on the RVE surfaces must be zero.

It has been shown that in an EFOCH extra boundary conditions must be considered. If the natural extension of the first average theorem is used (40) extra high-order conditions (50) are obtained. In consequence, this kind of boundary conditions require a high-order microscopic BVP. To avoid this situation, in this work will be used the conditions obtained for the alternative extension given by (57). Therefore, a first-order microscopic BVP is conserved in the RVE, as it will be shown in Sect. 3.3.

3.2 Microscopic and Macroscopic Strain Tensor

For an infinitesimal deformation approach, $\mathbf{E}_\mu$ can be written as

$$\begin{aligned}
\mathbf{E}_\mu(\mathbf{X}_o, \mathbf{X}_\mu) &= \frac{1}{2} \left(\mathbf{F}_\mu(\mathbf{X}_o, \mathbf{X}_\mu) + \mathbf{F}_\mu^T(\mathbf{X}_o, \mathbf{X}_\mu) \right) - \mathbf{I} \\
&= \frac{1}{2} \left(\mathbf{F}(\mathbf{X}_o) + \mathbf{F}^T(\mathbf{X}_o) \right) - \mathbf{I} \\
&\quad + \frac{1}{2} \left(\mathbf{G}(\mathbf{X}_o) \cdot \mathbf{X}_\mu + \left(\mathbf{G}(\mathbf{X}_o) \cdot \mathbf{X}_\mu \right)^T \right) \\
&\quad + \frac{1}{2} \left(\nabla \mathbf{w}(\mathbf{X}_\mu) + \left(\nabla \mathbf{w}(\mathbf{X}_\mu) \right)^T \right).
\end{aligned} \tag{62}$$

Knowing that (10) is satisfied and using (39), the resulting expression of the volume average of $\mathbf{E}_\mu$ over the RVE

domain is the same than (23), which was obtained previously in Sect. 2.1.3. Therefore, $\mathbf{E}_\mu$ can be rewritten as

$$\mathbf{E}_\mu(\mathbf{X}_o, \mathbf{X}_\mu) = \mathbf{E}(\mathbf{X}_o) + \mathbf{E}_\mu^G(\mathbf{X}_o, \mathbf{X}_\mu) + \mathbf{E}_\mu^w(\mathbf{X}_\mu), \tag{63}$$

where $\mathbf{E}_\mu^G = \frac{1}{2} \left(\mathbf{G} \cdot \mathbf{X}_\mu + \left(\mathbf{G} \cdot \mathbf{X}_\mu \right)^T \right)$ is a new term in the microscopic strain tensor, resulting from including the second-order term **G** in the formulation. Using the expression given by (39), it can be proved that the volume average of this new term $\mathbf{E}_\mu^G$ over the RVE domain is equal to zero.

3.3 Hill–Mandel Principle and RVE Equilibrium

When the second-order of the Taylor series expansion given by (3) is used to improve the approximation of the deformed position of a material point in the RVE (see 34), it is assumed that exists a macroscopic finite volume Ω_M around the considered point $\mathbf{X}_o$, as it is shown in Fig. 5. This finite volume must be smaller than the characteristic macroscopic dimension. Therefore, the Hill–Mandel principle [43, 68] should be applied now, not only taking into account the virtual work of the point $\mathbf{X}_o$, but considering the volume average of the virtual work in the macro volume Ω_M. This can be stated as

$$\frac{1}{V_M} \int_{\Omega_M} \mathbf{S} : \delta \mathbf{E} \, dV = \frac{1}{V_\mu} \int_{\Omega_\mu} \mathbf{S}_\mu : \delta \mathbf{E}_\mu \, dV \tag{64}$$

The macroscopic deformed position of a material point in Ω_M around the point $\mathbf{X}_o$ must now be approximated with a second-order approach using (3) as

$$\Delta \mathbf{x} \cong \mathbf{F}(\mathbf{X}_o) \cdot \Delta \mathbf{X} + \frac{1}{2} \mathbf{G}(\mathbf{X}_o) : \Delta \mathbf{X} \otimes \Delta \mathbf{X}, \tag{65}$$

and the approximated macroscopic deformation gradient is

$$\mathbf{F} \cong \mathbf{F}(\mathbf{X}_o) + \mathbf{G}(\mathbf{X}_o) \cdot \Delta \mathbf{X}. \tag{66}$$

The macroscopic strain tensor in the Ω_M domain for infinitesimal deformation approach can be then approximated as
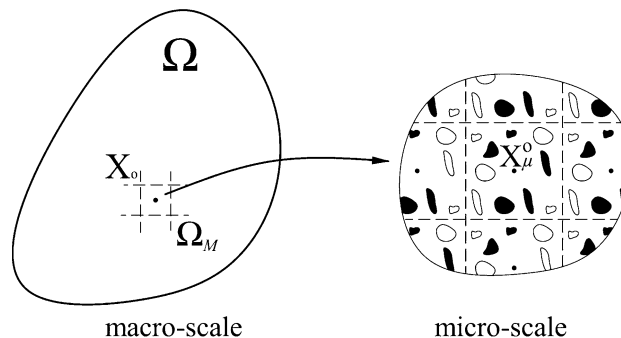

Fig. 5 Macro volume Ω_M around point $\mathbf{X}_o$ and its micro structure

$$\mathbf{E} \cong \frac{1}{2}\left(\mathbf{F}(\mathbf{X}_o) + \mathbf{F}^T(\mathbf{X}_o)\right) - \mathbf{I}$$
$$+ \frac{1}{2}\left(\mathbf{G}(\mathbf{X}_o) \cdot \Delta\mathbf{X} + (\mathbf{G}(\mathbf{X}_o) \cdot \Delta\mathbf{X})^T\right) \tag{67}$$

or

$$\mathbf{E} \cong \mathbf{E}(\mathbf{X}_o) + \mathbf{E}^G(\mathbf{X}_o, \mathbf{X}), \tag{68}$$

where $\mathbf{E}^G = \frac{1}{2}\left(\mathbf{G} \cdot \Delta\mathbf{X} + (\mathbf{G} \cdot \Delta\mathbf{X})^T\right)$.

Taking into account (63) and (68), the expression given by (64) can be rewritten as

$$\frac{1}{V_M}\int_{\Omega_M}\mathbf{S}\,dV : \delta\mathbf{E} + \frac{1}{V_M}\int_{\Omega_M}\mathbf{S} : \delta\mathbf{E}^G\,dV$$
$$= \frac{1}{V_\mu}\int_{\Omega_\mu}\mathbf{S}_\mu\,dV : \delta\mathbf{E} + \frac{1}{V_\mu}\int_{\Omega_\mu}\mathbf{S}_\mu : \delta\mathbf{E}_\mu^G\,dV \tag{69}$$
$$+ \frac{1}{V_\mu}\int_{\Omega_\mu}\mathbf{S}_\mu : \delta\mathbf{E}_\mu^w\,dV,$$

and because of the symmetry of $\mathbf{S}$, it can be proved that $\mathbf{S} : (\nabla\mathbf{a}) = \mathbf{S} : (\nabla\mathbf{a})^T$ and $\mathbf{S} : (\mathbf{G}.\mathbf{a}) = \mathbf{S} : (\mathbf{G}.\mathbf{a})^T$, where $\mathbf{a}$ is a first order tensor. Then, (69) is finally

$$\frac{1}{V_M}\int_{\Omega_M}\mathbf{S}\,dV : \delta\mathbf{E} + \frac{1}{V_M}\int_{\Omega_M}\mathbf{S}\otimes\Delta\mathbf{X}\,dV \vdots \delta\mathbf{G}$$
$$= \frac{1}{V_\mu}\int_{\Omega_\mu}\mathbf{S}_\mu\,dV : \delta\mathbf{E} + \frac{1}{V_\mu}\int_{\Omega_\mu}\mathbf{S}_\mu\otimes\mathbf{X}_\mu\,dV \vdots \delta\mathbf{G}$$
$$+ \frac{1}{V_\mu}\int_{\Omega_\mu}\mathbf{S}_\mu : \nabla^s\delta\mathbf{w}\,dV. \tag{70}$$

Following the same procedure used in Sect. 2.1.4 to satisfy the Hill–Mandel principle, it is necessary to define the following tensors:

$$\hat{\mathbf{S}} \equiv \frac{1}{V_M}\int_{\Omega_M}\mathbf{S}\,dV \equiv \frac{1}{V_\mu}\int_{\Omega_\mu}\mathbf{S}_\mu\,dV, \tag{71}$$

where $\hat{\mathbf{S}}$ is the homogenized stress tenor, which is obtained as the volume average of the stress tensor around the point $\mathbf{X}_o$, and

$$\hat{\mathbf{Q}} \equiv \frac{1}{V_M}\int_{\Omega_M}\mathbf{S}\otimes\Delta\mathbf{X}\,dV \equiv \frac{1}{V_\mu}\int_{\Omega_\mu}\mathbf{S}_\mu\otimes\mathbf{X}_\mu\,dV. \tag{72}$$

where $\hat{\mathbf{Q}}$ is the homogenized second-order stress tensor in the point $\mathbf{X}_o$, which is a third-order tensor. Finally, the RVE's variational equilibrium equation is

$$\int_{\Omega_\mu}\mathbf{S}_\mu : \nabla^s\delta\mathbf{w}\,dV = 0, \tag{73}$$

that must be satisfied for any kinematically admissible $\mathbf{w}$ shown in Sect. 3.1.

3.4 Homogenized Stress and Second-Order Stress Tensor

The microscopic stress tensor can be obtained as

$$\mathbf{S}_\mu = \mathbf{C}_\mu : \mathbf{E}(\mathbf{X}_o) + \mathbf{C}_\mu : \mathbf{E}_\mu^G(\mathbf{X}_o, \mathbf{X}_\mu)$$
$$+ \mathbf{C}_\mu : \mathbf{E}_\mu^w(\mathbf{X}_\mu), \tag{74}$$

then, $\hat{\mathbf{S}}$ at the macroscopic scale given by (71) is

$$\hat{\mathbf{S}} = \frac{1}{V_\mu}\int_{\Omega_\mu}\mathbf{C}_\mu\,dV : \mathbf{E}(\mathbf{X}_o)$$
$$+ \frac{1}{V_\mu}\int_{\Omega_\mu}\mathbf{C}_\mu : \mathbf{E}_\mu^G(\mathbf{X}_o, \mathbf{X}_\mu)\,dV \tag{75}$$
$$+ \frac{1}{V_\mu}\int_{\Omega_\mu}\mathbf{C}_\mu : \mathbf{E}_\mu^w(\mathbf{X}_\mu)\,dV$$

or

$$\hat{\mathbf{S}} = \bar{\mathbf{C}} : \mathbf{E}(\mathbf{X}_o) + \bar{\mathbf{B}} \vdots \mathbf{G}(\mathbf{X}_o)$$
$$+ \frac{1}{V_\mu}\int_{\Omega_\mu}\mathbf{C}_\mu : \mathbf{E}_\mu^w(\mathbf{X}_\mu)\,dV, \tag{76}$$

where

$$\bar{\mathbf{B}} \equiv \frac{1}{V_\mu}\int_{\Omega_\mu}\mathbf{C}_\mu\otimes\mathbf{X}_\mu\,dV. \tag{77}$$

The tensor $\bar{\mathbf{B}}$ can be considered a material property which relates $\mathbf{G}$ with $\hat{\mathbf{S}}$, and generates a coupling effect. This constitutive tensor is analogous to the called *bending-extension coupling matrix* used in plates or shells theories [2].

Equation (76) shows that $\hat{\mathbf{S}}$ in the point $\mathbf{X}_o$ depends of the macroscopic $\mathbf{E}$ and $\mathbf{G}$, of the microscopic $\mathbf{w}$ and also, of the position $\mathbf{X}_\mu$ of the RVE. Considering now a particular case where the simple materials within the RVE are symmetrically located respect to the coordinate system's origin, which has been placed on the RVE geometric center (see Sect. 3.1). It can be proved that taking this symmetric distribution of the simple materials the value obtains for $\bar{\mathbf{B}}$ is zero. Therefore, $\hat{\mathbf{S}}$ for this case can be rewritten as

$$\hat{\mathbf{S}} = \bar{\mathbf{C}} : \mathbf{E}(\mathbf{X}_o) + \frac{1}{V_\mu}\int_{\Omega_\mu}\mathbf{C}_\mu : \mathbf{E}_\mu^w(\mathbf{X}_\mu)\,dV. \tag{78}$$

Now, the term $\mathbf{G}$ and the position $\mathbf{X}_\mu$ do not affect $\hat{\mathbf{S}}$, and expression given by (78) is the same than the one obtained for FOCH given by (32).

On the other hand, the homogenized second-order stress tensor can be obtained using (72) and $\mathbf{S}_\mu$ given by (74) as

$$
\begin{aligned}
\hat{\mathbf{Q}} = &\frac{1}{V_\mu} \int_{\Omega_\mu} \mathbf{C}_\mu \otimes \mathbf{X}_\mu \, dV : \mathbf{E}(\mathbf{X}_o) \\
&+ \frac{1}{V_\mu} \int_{\Omega_\mu} (\mathbf{C}_\mu \otimes \mathbf{X}_\mu) : \mathbf{E}_\mu^G (\mathbf{X}_o, \mathbf{X}_\mu) \, dV \\
&+ \frac{1}{V_\mu} \int_{\Omega_\mu} \mathbf{C}_\mu : \mathbf{E}_\mu^w (\mathbf{X}_\mu) \otimes \mathbf{X}_\mu \, dV,
\end{aligned}
\tag{79}
$$

or

$$
\hat{\mathbf{Q}} = \bar{\mathbf{B}} : \mathbf{E}(\mathbf{X}_o) + \bar{\mathbf{D}} \vdots \mathbf{G}(\mathbf{X}_o) + \frac{1}{V_\mu} \int_{\Omega_\mu} \mathbf{C}_\mu : \mathbf{E}_\mu^w (\mathbf{X}_\mu) \otimes \mathbf{X}_\mu \, dV,
\tag{80}
$$

where

$$
\bar{\mathbf{D}} = \frac{1}{V_\mu} \int_{\Omega_\mu} (\mathbf{C}_\mu \otimes \mathbf{X}_\mu) \otimes \mathbf{X}_\mu \, dV.
\tag{81}
$$

The tensor $\bar{\mathbf{D}}$ is also considered a material property, which is obtained with the RVE model, as it is done with tensors $\bar{\mathbf{C}}$ and $\bar{\mathbf{B}}$. Taking into account the symmetric materials distribution inside the RVE, the expression for $\hat{\mathbf{Q}}$ can be rewritten as

$$
\hat{\mathbf{Q}} = \bar{\mathbf{D}} \vdots \mathbf{G}(\mathbf{X}_o) + \frac{1}{V_\mu} \int_{\Omega_\mu} \mathbf{C}_\mu : \mathbf{E}_\mu^w (\mathbf{X}_\mu) \otimes \mathbf{X}_\mu \, dV.
\tag{82}
$$

Equation (82) shows that $\hat{\mathbf{Q}}$ depends on the macroscopic $\mathbf{G}$ and on the microscopic $\mathbf{w}$. But it also depends on the position $\mathbf{X}_\mu$ of the material point in the RVE. In addition, the tensor $\bar{\mathbf{D}}$ does not vanish because of the symmetric materials distribution.

3.5 Some Remarks of the EFOCH

In the proposed EFOCH is lost the benefit shown by the FOCH regarding the possibility of using a non-dimensional RVE. Now, the microscopic strain (63) and stress (74) tensor have an explicit dependence with the position $\mathbf{X}_\mu$ in the RVE. Besides, to satisfy (69), which is obtained from the Hill–Mandel condition, it is necessary to impose that $\Omega_\mu \equiv \Omega_M$. Thus the RVE's dimension used to characterize the microstructure should be equal to the size of the finite volume around the considered point $\mathbf{X}_o$.

On the other hand, a detailed analysis of the EFOCH formulation shows that the FOCH is contained in it. Therefore, when the principle of separation of scales is satisfied ($l \gg l_\mu$), the results given by the EFOCH will be the same than the ones provided by the FOCH.

As will be shown in the next section, the EFOCH conserves the classical first-order BVP in the structural level.

Therefore, the macroscopic second-order stress tensor obtained from the RVE solution is not considered in the macroscopic problem. This restricts the use of the EFOCH to analyses where the principle of separation of scales is satisfied or moderately satisfied. When this principle is not verified, the homogenized tensor $\hat{\mathbf{Q}}$ should be considered in the macroscopic BVP as the SOCH does [29, 60, 61].

However, from a microscopic point of view, the results of the EFOCH are better than the ones provided with the FOCH. Although the macroscopic stress tensor obtained for both theories is the same, the microscopic displacement field, the strain and, the stress tensors are not equal. The EFOCH obtains a better approximation of the microscopic behavior. Therefore, in a non-linear analysis, the initiation and the evolution of the non-linear performance of the microstructure will be better characterized.

4 Formulation and Numerical Implementation

In the following, the macroscopic and microscopic BVPs are presented.

4.1 Macroscopic BVP

A macrostructural scale of domain Ω with a periodic internal microstructure is considered. The kinematics of the problem is related to a displacement field on the macroscopic scale, which provides the displacement of each material point in Ω. From a continuum mechanics approach the macroscopic BVP is

$$
\begin{aligned}
\frac{\partial S_{ij}}{\partial X_j} + f_i = 0 \quad &in \quad \Omega, \\
u_i = \bar{u}_i \quad &in \quad \partial\Omega_u, \\
S_{ij} N_j = \bar{t}_i \quad &in \quad \partial\Omega_t,
\end{aligned}
\tag{83}
$$

where S_{ij} is the macroscopic stress tensor, and f_i is the internal body force associated to the mass force of the material. The boundary of $\Omega(\partial\Omega)$ is defined disjointedly by the surfaces $\partial\Omega_u$ where the macroscopic displacement is known $\bar{u}_i$ (Dirichlet's condition) and $\partial\Omega_t$ where the macroscopic surface load $\bar{t}_i$ is known (Neumann's condition) with $\partial\Omega_u \cup \partial\Omega_t = \partial\Omega$ and $\partial\Omega_u \cap \partial\Omega_t = \emptyset$. Finally, N_j are the components of an outward vector normal to the surface $\partial\Omega_t$.

The resolution of the BVP given by (83) consists on the determination of the macroscopic displacement field corresponding to the solution $\mathbf{u} \in V_\Omega$, where V_Ω is the set of continuous and sufficiently regular functions with zero-value in $\partial\Omega_u$. The partial differential equation in the macroscopic BVP presented above can be rewritten in a weak form (or variational form) as

$$\int_\Omega \frac{\partial S_{ij}}{\partial X_j} v_i \, dV + \int_\Omega f_i v_i \, dV = 0 \qquad \forall \, v \in V_\Omega, \tag{84}$$

where v_i are the called test functions. Equation (84) can be rewritten, applying the divergence theorem, as

$$\int_\Omega S_{ij} \frac{\partial v_i}{\partial X_j} \, dV = \int_\Omega f_i v_i \, dV + \int_{\partial\Omega} \bar{t}_i v_i \, dA \quad \forall \, v \in V_\Omega. \tag{85}$$

Considering infinitesimal deformations, the macroscopic strain and stress tensor are

$$\begin{aligned}
E_{ij} &= \frac{1}{2}\left(F_{ij} + F_{ij}^T\right) - I_{ij} = \frac{1}{2}\left(\frac{\partial u_i}{\partial X_j} + \frac{\partial u_j}{\partial X_i}\right) \quad in \; \Omega, \\
S_{ij} &= \frac{1}{V_\mu} \int_{\Omega_\mu} S_\mu \, dV \quad in \quad \Omega.
\end{aligned} \tag{86}$$

4.2 Microscopic BVP

The variational equilibrium statement (or the virtual work equation) in the microstructure (see 29 and 73) can be written as

$$\int_{\Omega_\mu} S_\mu : \nabla^s w \, dV = 0 \qquad \forall \, w \in V_{\Omega_\mu}. \tag{87}$$

Considering again an infinitesimal deformation, the microscopic strain tensor is

$$E_\mu = \frac{1}{2}\left(F_\mu + F_\mu^T\right) - I = \nabla^s u_\mu \, in \, \Omega_\mu, \tag{88}$$

where $\nabla^s u_\mu$ is the symmetric gradient of the microscopic displacement field in the RVE and V_{Ω_μ} is the set of continuous and sufficiently regular kinematically admissible RVE displacement fields. Further, it is assumed that in the microstructure the constitutive behavior is described by conventional internal dissipative constitutive theories. Therefore, the microscopic stress tensor is obtained by integrating the constitutive equations, knowing a set of internal variables $\boldsymbol{\alpha}$, for the given strain tensor history. Then, it is

$$S_\mu = S_\mu(E_\mu, \boldsymbol{\alpha}) = S_\mu(\nabla^s u_\mu, \boldsymbol{\alpha}). \tag{89}$$

With the above at hand, the resolution of the problem consists on the determination of $u_\mu \in V_{\Omega_\mu}$ of the variational problem for a given macroscopic tensor F, and its gradient G in EFOCH. Therefore, to complete the microscopic BVP it is necessary to define the boundary conditions used to obtain kinematically admissible displacement fields from the solution of (87).

4.2.1 Consequence of the Boundary Conditions Selected

The RVE has a finite dimension, which is opposed to the theoretically infinite microstructure usually considered.

This creates the intrinsic problem of the non-physical RVE edges. As a result, the election of the boundary condition in the RVE problem is essential to characterize the real behavior of the microstructure.

It has been shown in Sect. 2.1.5 that the boundary condition used in the RVE problem affects the macroscopic stress tensor obtained and therefore it also affects the homogenized constitutive tensor. In example, the expression (32) shows that using the *Taylor model* condition the result provides an upper bound of the estimated homogenized microscopic stiffness.

On the other hand, the *Minimal constraint* provides a lower bound of the estimated effective microstructural stiffness. This boundary condition imposes the macroscopic strain tensor on the RVE in the weakest sense. It has been shown that the resulting boundary distribution of the microscopic stress tensor in the RVE is uniform and equal to the macroscopic stress tensor in this boundary restriction [15, 74].

The *Linear boundary displacements* condition is a too restrictive constraint and it overestimates the homogenized microscopic stiffness [13]. A conventional BVP with full Dirichlet's condition is obtained for the RVE.

It is shown in literature that the *Periodic boundary fluctuations* provide a better apparent stiffness estimation for both periodic as well as random microstructures [52, 53, 74, 76, 97, 120, 126]. This condition makes the RVE self adjoint by point to point (pairs of points) coupling of boundary displacements, thereby it naturally incorporates the mechanical response of the surrounding material. Moreover, an anti-periodic condition of the boundary forces is automatically fulfilled in the problem because the boundary points of the RVE are considered as internal points of the structure.

Based on the different performances described, in this work the *Periodic boundary fluctuations* condition will be used in the computational implementation for both approaches considered, FOCH and EFOCH.

FOCH case In Sect. 2.1.2, the *Periodic boundary fluctuations* condition was obtained (see 21). Using (9) is possible to obtain this in terms of u_μ as

$$\begin{aligned}
&u_\mu(X_\mu^+) - u_\mu(X_\mu^-) = D_i(F - I) \cdot N_i^+, \\
&\forall \, pairs \left\{ X_\mu^+, X_\mu^- \right\} \in \partial\Omega_{\mu|N_i}; \quad i = X,Y,Z.
\end{aligned} \tag{90}$$

EFOCH case. The *Periodic boundary fluctuations* condition was obtained in Sect. 3.1. Now, using (36) is possible to write this in terms of u_μ as

$$\begin{aligned}
&u_\mu(X_\mu^+) - u_\mu(X_\mu^-) = D_i(F - I) \cdot N_i^+ + \frac{D_i^2}{2} G : N_i^+ \otimes N_i^+ \\
&\quad + D_i G : N_i^+ \otimes X_\mu^-, \\
&\forall \, pairs \left\{ X_\mu^+, X_\mu^- \right\} \in \partial\Omega_{\mu|N_i}; \quad i = X,Y,Z.
\end{aligned} \tag{91}$$

In this case, the extra boundary restriction due to the introduction of term $\mathbf{G}$, for this kind of boundary condition (see 61) is written in terms of $\mathbf{u}_\mu$ as

$$
\begin{aligned}
\frac{2}{V_\mu} \int_{\mathbf{N}_i^-} \mathbf{u}_\mu \, dA &= (\mathbf{I} - \mathbf{F}) \cdot \mathbf{N}_i^+ + \frac{D_i}{4} \mathbf{G} : \mathbf{N}_i^+ \otimes \mathbf{N}_i^+ \\
&\quad + \frac{D_j^2}{12 D_i} \mathbf{G} : \mathbf{N}_j^+ \otimes \mathbf{N}_j^+ + \frac{D_k^2}{12 D_i} \mathbf{G} : \mathbf{N}_k^+ \otimes \mathbf{N}_k^+, \\
&\qquad\qquad\qquad\qquad i = X \Rightarrow j = Y, k = Z \\
\forall \mathbf{X}_\mu \in \partial\Omega_{\mu|\mathbf{N}_i^-}; &\qquad i = Y \Rightarrow j = X, k = Z \\
&\qquad\qquad\qquad\qquad i = Z \Rightarrow j = X, k = Y
\end{aligned} \tag{92}
$$

which are integral constraint boundary conditions.

4.3 Numerical Implementation

The numerical solution of the presented BVPs are obtained through the FEM. To solve the macroscopic BVP it will be necessary to know the stress tensor in the macro domain. The multiscale computational homogenization methods above described are used as constitutive models of the heterogeneous material. Therefore, the macroscopic $\mathbf{F}$, for the FOCH, and its gradient $\mathbf{G}$, for the EFOCH, are used to solve the microscopic BVP. Consequently, the homogenized stress tensor necessary to solve the macroscopic BVP is obtained from the solution of this microscopic problem.

The proposed EFOCH has been implemented in PLCd [92, 99], a parallel FE code that works with 3D solid geometries. The PLCd program has already implemented the FOCH described previously [93, 94]. The microscopic displacement field obtained from the solution of the microscopic BVP must satisfy the boundary conditions defined previously, in Sect. 4.2.1. The restrictions of degrees of freedom on the RVE boundary domain is imposed by an elimination of redundant unknowns [34, 94]. Equations (90), (91) and (92) show the redundant boundary unknowns. In these expressions it is possible identify master unknowns (the unknowns to solve) and slave unknowns [92]. In "Appendix", the master-slave kinematic relationships are presented for the EFOCH.

4.4 Some Important Considerations

Based on the characteristics of the formulations developed, as well as on the implementation of these formulations using the finite element method, in the following are included some final remarks regarding the implications of using the FOCH or the EFOCH.

Let us assume, for the sake of simplicity that the macroscopic FE mesh has a single integration point. In this case, the macroscopic finite volume Ω_M around the considered point $\mathbf{X}_o$ in the formulation is related with the FE domain as $\Omega_e = \Omega_M$, where Ω_e is the FE domain. Taking into account the considerations made in Sect. 3.5 it can be concluded that $\Omega_e = \Omega_\mu$, which means that for the integration point of the FE, the RVE domain must be geometrically equal to the FE domain. Consequently, in the EFOCH the RVE dimension is related with the discretization mesh used in the macroscopic BVP.

The macroscopic BVP presented in Sect. 4.1 does not take into account the homogenized second-order stress tensor $\hat{\mathbf{Q}}$ obtained in the enhanced-first-order homogenization. Besides, if the RVE materials are symmetrically distributed in it, the estimated homogenized stress tensor obtained is the same for both homogenization approaches. Therefore, the proposed EFOCH does not improve the macroscopic results obtained from the BVP. To improve these, a high-order FE or enhanced FE mesh must be considered at the structural scale. To account for the homogenized second-order stress tensor $\hat{\mathbf{Q}}$ in the macroscopic scale a SOCH must be used [29, 60, 61].

4.5 Linear FE in the Macroscopic Mesh

In linear finite element the interpolation functions are first-order polynomials and consequently, the displacement field in the domain of the FE is a first-order function. The strain tensor is obtained by differentiating the displacement field, then the strain tensor in the FE will be a constant function. Therefore, a fine FE mesh on the macroscopic BVP should be used to obtain an accurate approximation of the strains and stresses.

When linear finite elements and a FOCH are used to solve the macroscopic problem, the RVE is just a representative sub-domain of the periodic microstructure that does not have any significance on real microscopic dimension as has been shown in Sect. 2.1.5. The constant value of the macroscopic gradient tensor $\mathbf{F}$ in the integration point of the macroscopic FE is used to define the BVP in the RVE. From the solution of the microscopic problem the macroscopic stress tensor is obtained for the considered integration point.

In linear FE case, the solution of the microscopic BVP with the EFOCH is an inefficient procedure because the value of $\mathbf{G}$ in the integration point of the macroscopic linear element has partial or even zero information.

4.6 High-Order FE in the Macroscopic Mesh

To improve the FEM approach high-order elements can be used. Quadratic finite elements use second-order polynomials as interpolation functions to approximate the displacement field within the FE's domain. The deformation gradient tensor $\mathbf{F}$ of this element is a first-order function,

while gradient of the deformation gradient tensor $\mathbf{G}$, which is obtained deriving twice the displacement, is a constant function on the FE domain.

The developed EFOCH needs at least quadratic elements in the macroscopic mesh in order for the functions $\mathbf{F}$ and $\mathbf{G}$ not to have zero value in the FE domain. Quadratic elements need more than one Gauss point to obtain the best integration approximation. As mentioned before, in the proposed homogenization method the RVE dimension must be related with the FE dimension. Therefore, for quadratic elements the RVE must represent the sub-domain within the FE associated to the Gauss point. If not, the analysis will have an associated error due to the size mismatch.

For this case, the best approximation of the strain and stress fields at the micro-scale is obtained through an EFOCH together with a RVE which represents the real volume of the surrounding domain in the Gauss point. The numerical examples described in Sect. 5 show that the EFOCH produces more realistic stress fields at the micro-scale which will lead to a better material characterization, specially if non-linear effects are taken into account.

5 Numerical Example

The objective is this section to show the advantages and drawbacks of the EFOCH with respect to the FOCH through numerical examples.

Two numerical examples have been analyzed with the same macroscopic geometry, the first one uses a homogeneous material. In this case, the numerical results can be compared with the existing analytical solution. The second numerical simulation uses a matrix with a long fiber reinforcement.

5.1 Geometry, Boundary Conditions and Mesh Information

5.1.1 Macroscopic Beam Model

The macroscopic structure chosen is a three-dimensional fixed support beam that is subjected to a fixed displacement (d_Z) at the free end. Figure 6 shows the dimensions and the support scheme on the geometry of the beam.

To study the numerical stability and convergence of the problem four mesh sizes are simulated. Linear elements and quadratic elements are used in the different meshes of the numerical model for the FOCH case while only quadratic FEs are used for the EFOCH. The linear FE is an hexahedron of 8 nodes and 8 Gauss points, and the quadratic FE is an hexahedron with 20 nodes and 27 Gauss points.

Table 1 shows the more relevant information about the macroscopic meshes used. These meshes are also shown in Fig. 7.

5.1.2 Microscopic RVE Model

The geometry of the RVE depends of the numerical simulation case. For the case of a homogeneous material, the RVE is a simple cube with length L, this is shown in Fig. 8a. In the second simulation case, the material defined is a composite with a 40% of cylindrical long fiber volume. The geometry of the RVE that represents this periodical microstructure is shown in the Fig. 8b.

It has been shown in previous section that the dimension of the RVE is an important parameter for the EFOCH. Moreover, this dimension L is directly related with the volume around the Gauss point of the FE in the macroscopic mesh. Therefore, the value of the length L depends of the dimension of the macroscopic FE used and of the number of Gauss points of the FE. In Table 2 the number of elements in the beam height, Z direction, and the value that takes the length L in the RVE for the different macroscopic meshes used are shown. The value of the length L has been calculated considering quadratic elements on the macroscopic mesh.

The RVE has been analyzed with just one FE model. Figure 9a shows the mesh used in the RVE for the homogeneous material case, which has 1000 FE. Figure 9b
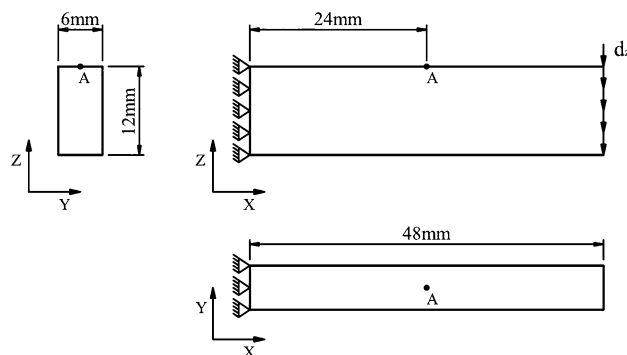
**Fig. 6** Dimensions of the geometry and support scheme of the structure simulated

Table 1 Number of elements (in X, Y and Z directions), nodes and Gauss points of the meshes used in the beam structure

Mesh	Elements	Linear elem.		Quadratic elem.	
		Nodes	Gauss	Nodes	Gauss
Macro1	$8 \times 1 \times 2$	54	128	165	432
Macro2	$16 \times 2 \times 4$	255	1024	869	3456
Macro3	$32 \times 4 \times 8$	1485	8192	5433	27,648
Macro4	$64 \times 8 \times 16$	9945	655,366	37,937	221,184

(a)

(b)

(c)

(d)
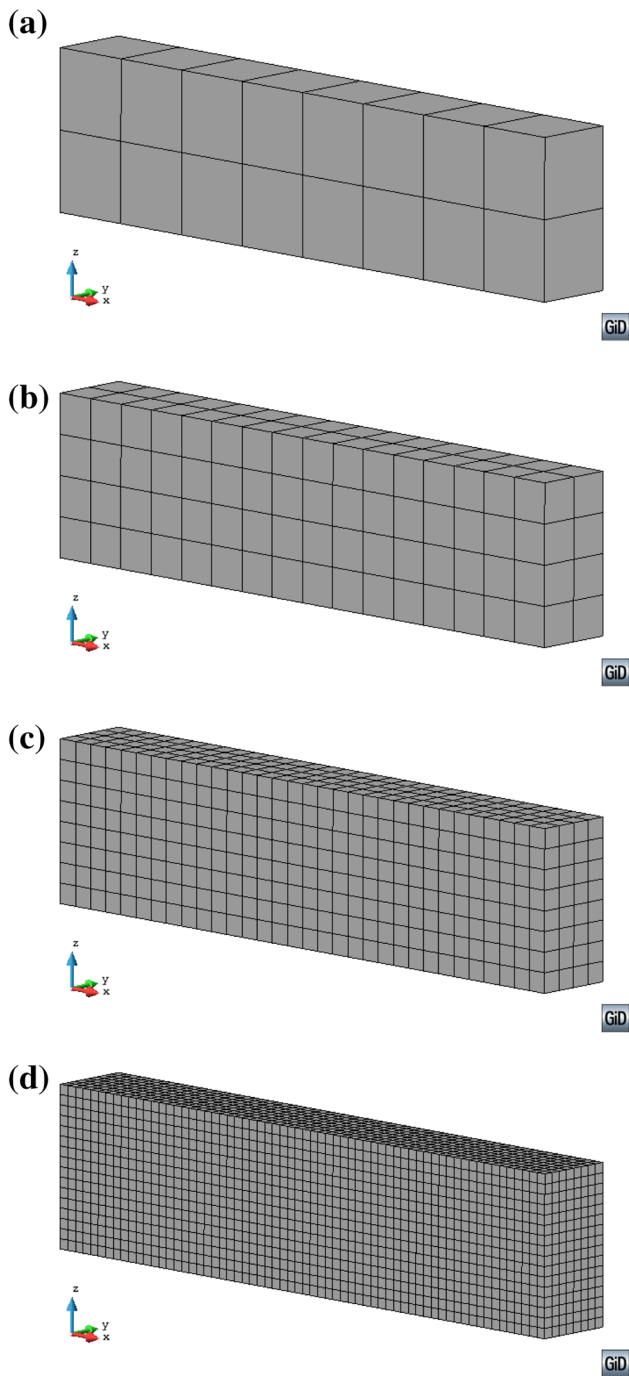
Fig. 7 Different mesh sizes used in the macroscopic numerical model. **a** Macro1, **b** Macro2, **c** Macro3, **d** Macro4

shows the mesh of the RVE for the composite material. In this case, it has 1936 FE. For both RVE meshes, the FEs used are linear.
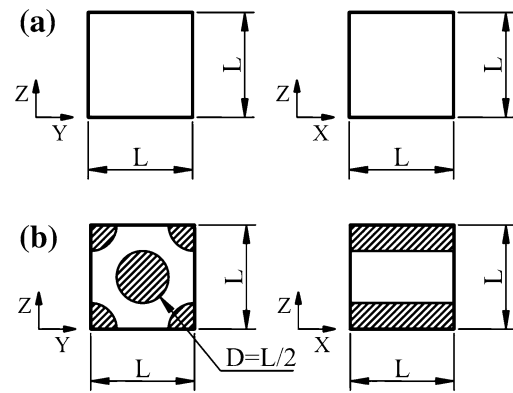
Fig. 8 RVE models for the two different numerical simulation cases **a** RVE for homogeneous material, **b** RVE for composite material

Table 2 Number of elements in Z direction of the beam and length L of the RVE for the different macroscopic mesh sizes

Data	Macro1	Macro2	Macro3	Macro4
Num. elem.	2	4	8	16
Length L [mm]	1.3525	0.6762	0.3381	0.1691
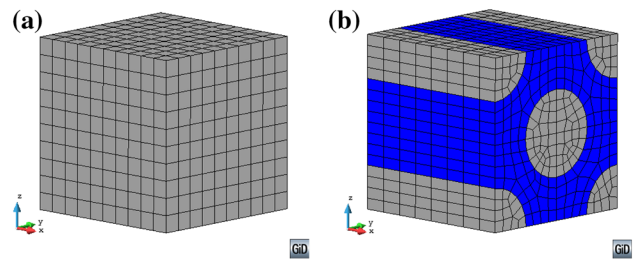
Fig. 9 Mesh used on the RVE models for the different numerical simulations **a** for homogeneous, **b** for composite

5.2 Results and Analysis

5.2.1 Checkpoints and Variables Compared in the Simulation

The reaction force in Z direction on the fixed support is a variable used for the comparison. To compare not only this macroscopic variable another checkpoint has been designed. The macroscopic stress value is compared in the macroscopic Gauss point closest to point A (see Fig. 6) and the microscopic stress obtained in the RVE is also compared for this same Gauss point. The microscopic stress value used for the comparison is the one obtained in the Gauss point closest to point A within the RVE. The geometric point A is shown in Fig. 6. The longitudinal stress

Table 3 Reaction force, longitudinal and shear stresses in point A of the analytical solution

Data	R_Z [N]	S_{XX} [MPa]	S_{XZ} [MPa]
Values	600	100	0

Table 4 Reaction force and relative error for the different approaches and meshes

R_Z [N]	Macro1	Macro2	Macro3	Macro4
LE&FO	679.09	620.03	605.09	601.34
% e_{rel}	13.18	3.34	0.85	0.22
QE&FO	600.43	600.12	600.09	600.08
% e_{rel}	0.07	0.02	0.01	0.01
QE&EFO	600.43	600.12	600.09	600.08
% e_{rel}	0.07	0.02	0.01	0.01

Table 5 Macroscopic longitudinal stress and relative error for the values obtained in the Gauss point closest to point A

S_{XX} [MPa]	Macro1	Macro2	Macro3	Macro4
LE&FO	69.43	84.02	91.82	95.86
% e_{rel}	30.57	15.98	8.18	4.14
QE&FO	86.08	93.00	96.50	98.25
% e_{rel}	13.92	7.00	3.50	1.75
QE&EFO	86.08	93.00	96.50	98.25
% e_{rel}	13.92	7.00	3.50	1.75

values (S_{XX}) and the shear stress values (S_{XZ}) will be compared on this point.

5.2.2 Homogeneous Material Simulation

When the material used in the beam is a homogeneous material it is possible to obtain the analytical solution for the support scheme shown in the Fig. 6. The reaction force in Z direction is given by

$$R_Z = \left[\frac{l^3}{3EI_{yy}} + \frac{6l}{5GA} \right]^{-1} d_Z, \qquad (93)$$

where E and G is the Young's modulus and shear modulus of the material, respectively, while I_{yy}, A and l are the second moment of area, the cross section area and the longitudinal length of the beam, respectively. Therefore, considering an isotropic material with null Poisson's ratio, $E = 26560$ [MPa], $G = 13280$ [MPa] and taking a fixed displacement of $d_Z = 1$ [mm], it is possible to address the values shown in Table 3 from the analytical solution. The S_{XX} and S_{XZ} values shown in table correspond to the analytical values obtained in point A.
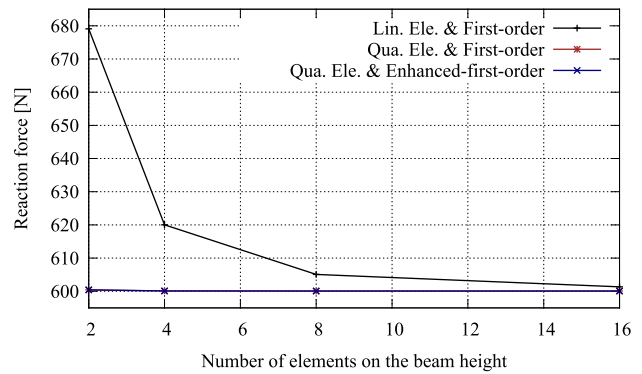
Fig. 10 Reaction force versus number of elements in Z direction for the different approaches

Table 6 Longitudinal stress in the RVE (Gauss point closest to point A) and relative error for the different approaches and meshes

S_{XX} [MPa]	Macro1	Macro2	Macro3	Macro4
LE&FO	69.43	84.02	91.82	95.86
% e_{rel}	30.57	15.98	8.18	4.14
QE&FO	86.08	93.00	96.50	98.25
% e_{rel}	13.92	7.00	3.50	1.75
QE&EFO	98.66	99.59	99.87	99.96
% e_{rel}	1.34	0.41	0.14	0.04
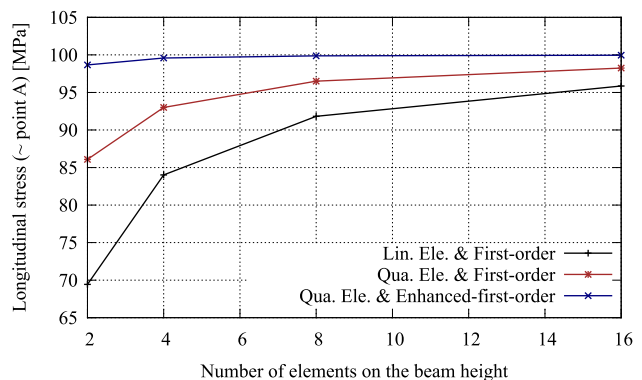
Fig. 11 S_{XX} obtained close to point A for the different meshes and approaches used

The numerical results obtained for the different approaches and meshes are presented in a simplified form using tables and graphs. On the tables, the relative error or absolute error obtained when comparing the result with the analytical solution is also shown.

Table 4 shows the reaction force in Z direction obtained with the numerical simulations. In this table, the results obtained with Linear Elements (LE) in the macro-model and the First-Order (FO) computational homogenization are shown in the first two rows. The following two rows show the results obtained with Quadratic Elements (QE)
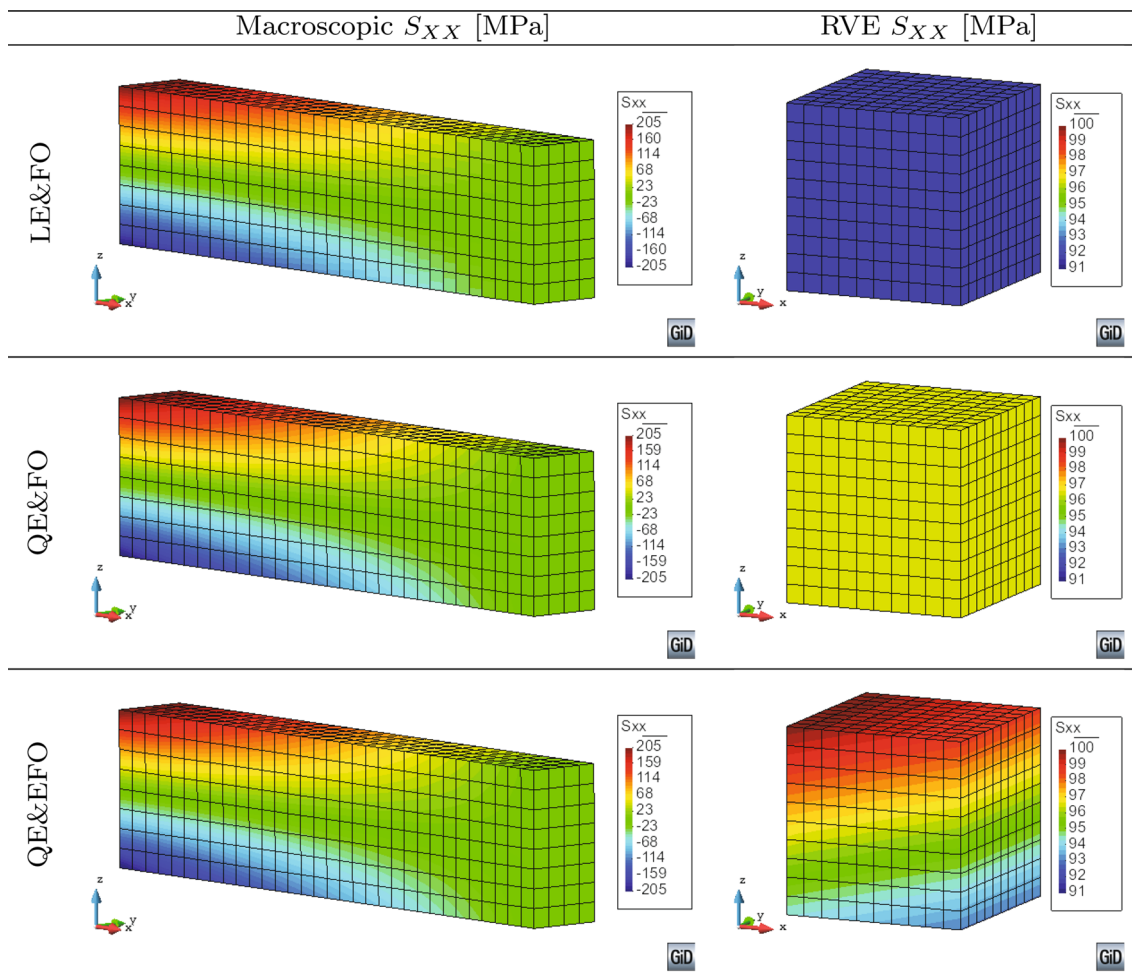
Fig. 12 Macroscopic and microscopic (RVE closest to point A) S_{XX} field for the mesh Macro3

Table 7 Microscopic shear stress (Gauss Point closest to point A) and absolute error for the different approaches and meshes

S_{XZ} [MPa]	Macro1	Macro2	Macro3	Macro4
LE&FO	−22.14	−12.26	−6.43	−3.29
QE&FO	−3.90	−1.68	−0.77	−0.37
QE&EFO	−1.88	−0.48	−0.13	−0.04

Fig. 13 S_{XZ} obtained close to point A for the different meshes and approaches used

and the FOCH. And, in the last two rows, are included the results obtained with QE for the macro model, and the Enhanced-First-Order (EFO) computational homogenization.

It is possible to observe that the results do not change when a EFOCH is used, if they are compared with the QE&FO results. This is because the EFOCH formulation does not improve the macroscopic solution. The macroscopic stress field obtained is the same than the one obtained with a FOCH approach, and therefore the reaction forces are also the same (see Table 5). Another interesting

conclusion obtained from the results is that an increase in the order of the macro FE represents a meaningful improvement. The mesh Macro1 with QE obtains best results than the mesh Macro4 with LE, which is surprising because Macro4 has 16 FE in the beam height. Figure 10

Table 8 Reaction force for the different approaches and meshes

R_Z [N]	LE&FO	QE&FO	QE&EFO
Macro1	1629.76	1537.74	1537.96
Macro2	1559.39	1530.45	1530.46
Macro3	1537.43	1529.36	1529.34
Macro4	1531.30	1529.10	1529.14
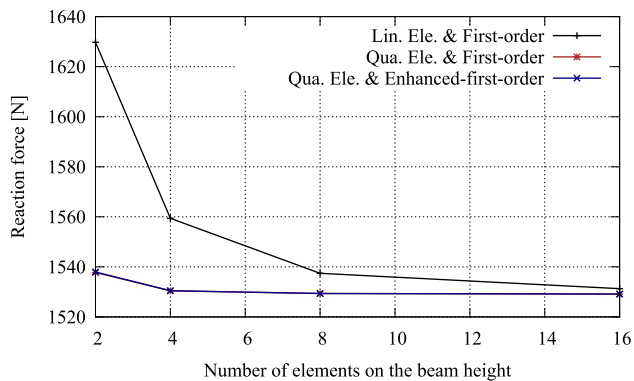
Fig. 14 Reaction force versus number of elements in Z direction for the different approaches

shows the curves of reaction force versus number of FEs in the beam height. This curve shows clearly the result previously addressed.

Table 5 shows the macroscopic longitudinal stress obtained from the numerical simulations and the relative error of these numerical results using the analytical result $S_{XX} = 100$ [MPa] as reference. The stress values shown in the table correspond to the ones obtained for the Gauss point closest to point A on the beam meshes. It has to be noted that for large meshes, the error is also increased because the position of the Gauss point, from which the numerical result is obtained, differs slightly from the position of point A.

The improvements of the EFOCH can be seen when comparing the microscopic results provided by the RVEs used in the macroscopic Gauss point closest to point A. The longitudinal stress and shear stress present in the following tables and figures are the microscopic stress values of the Gauss point in the RVE closest to point A. Table 6 shows the value of the longitudinal stress obtained within the RVE for the Gauss point closest to point A. This table shows that the results provided by the EFOCH are always closer to the analytical ones, as the model is capable of capturing the bending effects in the material.

Figure 11 shows the stress obtained as a function of the number of elements in the beam height. The general behavior of the stress when the number of elements increase is similar. When a EFOCH is used the estimation

of the stress is good even for large elements. Moreover, the benefit of change the approach is more significant for meshes with low number of elements. The relative error for 2 elements case is around 1% which represents a very good estimation.

As an example of the macroscopic and microscopic longitudinal stress field obtained for the different approaches Fig. 12 shows S_{XX} for the mesh case Macro3. For the FOCH the figure shows an uniform stress distribution in the RVE, this is because the formulation only uses the macroscopic deformation gradient to solve the RVE. This occurs independently of the macro elements uses, LE or QE. The macroscopic improvement observed in the QE model is because the solution of the macroscopic problem is better when this kind of element is used. For the same macroscopic solution, if an EFOCH is used, the approximation of the microscopic stress field improves. The RVE stress field shows a not uniform distribution (see QE&EFO case) because the EFOCH can considered second-order effects in the microstructure.

The results obtained for the shear stress in the RVE for the Gauss point closest to point A are shown in Table 7. This table does not show the relative error because for this variable the analytical value obtained in the geometric point A is $S_{XZ} = 0$ [MPa]. Figure 13 shows the shear stress obtained for the different approaches as a function of the number of elements in the height of the beam. From the table and the figure it is possible to observe that the main improvement in the shear stress results it is presented when the FE is changed. However, the use of the EFOCH improves the shear stress obtained for all meshes considered. The reason for this improvements is, as has been pointed out with the S_{XX} value, the capacity that the EFOCH gives to the RVE model to account for the second-order effects existing in the macro model.

5.2.3 Composite Material

In the following numerical simulations, the material used is a composite with long fibers. The RVE used to simulate the internal structure of this composite is shown in Fig. 8b, while the FE mesh used is shown in Fig. 9b. The material used for the matrix is an elastic isotropic material (resin epoxy HSC Epikote 4652) with a Young's modulus of $E_m = 4.52$ [GPa] and a Poisson's ratio of $v_m = 0.36$. The long fiber material considered is a carbon fiber (Grafil TR30S 3K carbon fiber) with a $E_f = 235$ [GPa] and $v_f = 0.21$. The materials properties have been taken from the work of Perez et al. [96].

Table 8 shows the Z direction reaction force obtained for the different approaches and meshes used in the

numerical simulation. Figure 14 shows these same reaction forces plotted against the number of elements on the beam height. This figure shows that the global performance

provided in the different models for the homogeneous material is also provided for the composite material. This is: changing the computational homogenization does not
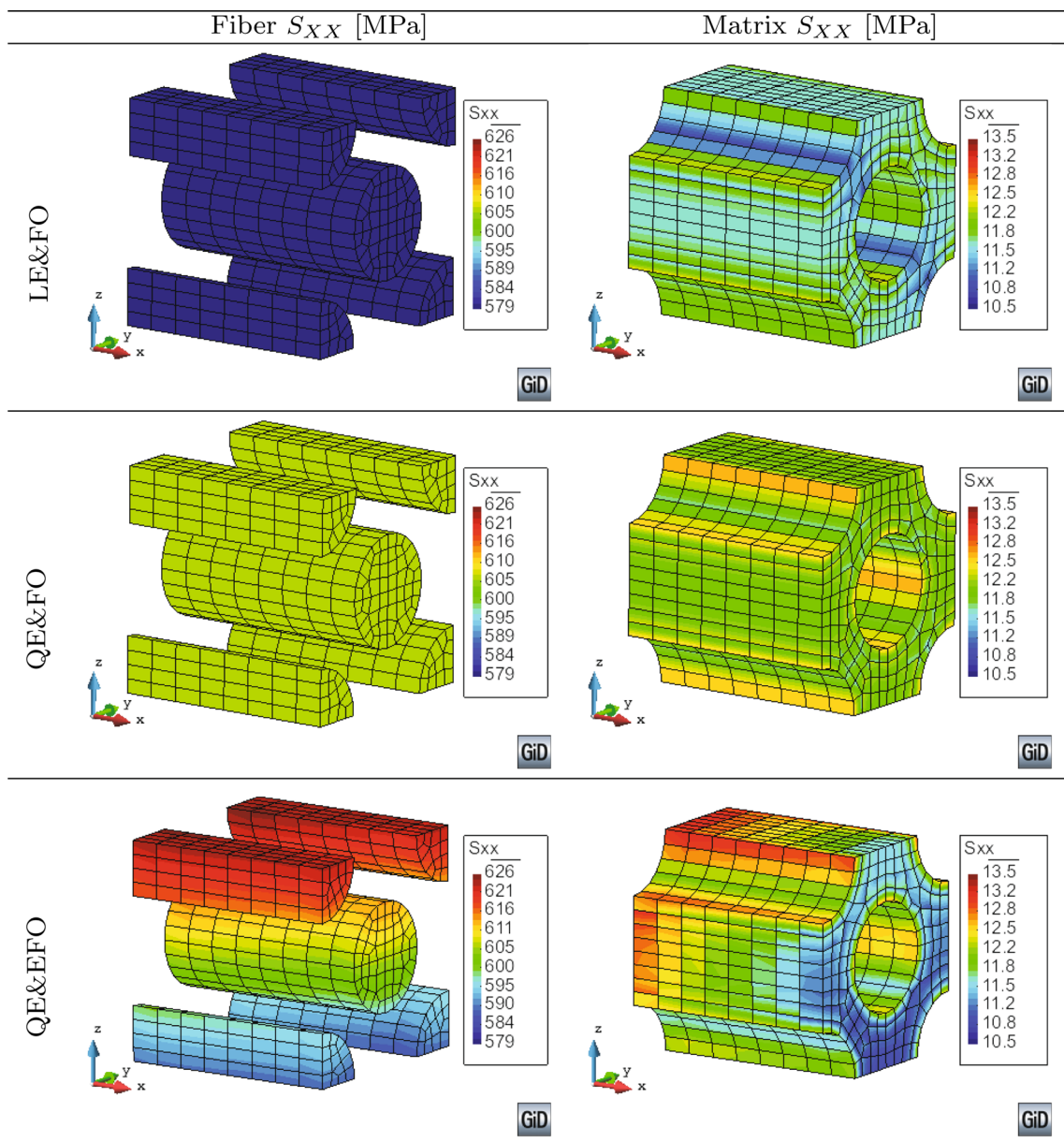
Fig. 15 Fiber and matrix longitudinal stress field in the RVE of the Gauss point closest to point A for the mesh Macro3

Table 9 S_{XX} of the components in the RVE for the different approaches and meshes

Data	Fiber S_{XX} [MPa]			Matrix S_{XX} [MPa]		
	LE&FO	QE&FO	QE&EFO	LE&FO	QE&FO	QE&EFO
Macro1	454.56	543.31	616.13	11.11	11.18	14.10
Macro2	534.71	584.90	622.41	11.69	12.01	13.67
Macro3	578.97	606.60	625.56	12.23	12.46	13.25
Macro4	603.02	617.54	627.07	12.53	12.68	12.98
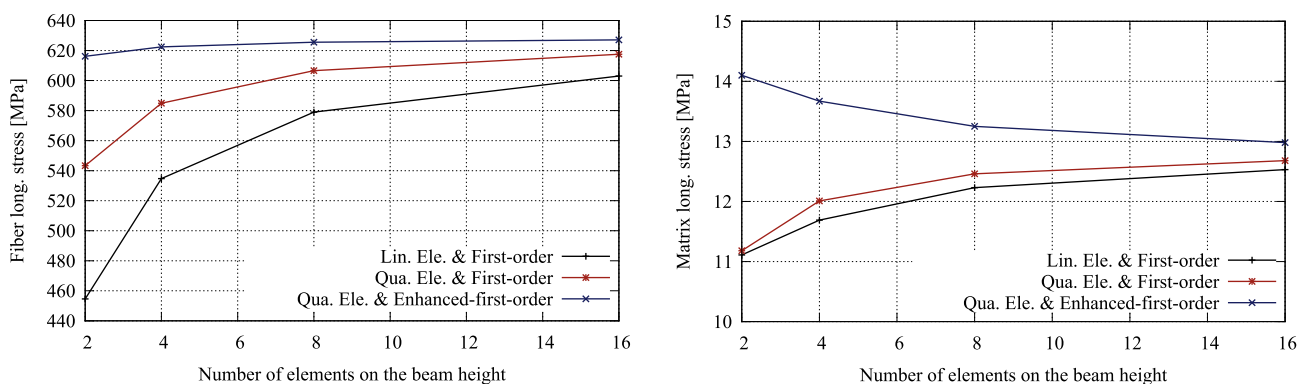
Fig. 16 Longitudinal stress of the fiber and matrix components in the RVE close to point A for the different meshes and approaches used

change the reaction force obtained and the use of QE represents a meaningful improvement of the results obtained.

The improvements on the microscopic results when an EFOCH is used can be seen in Fig. 15. The microscopic stress fields shown in the figures correspond to the RVE of the macroscopic Gauss point closest to point A for the beam mesh Macro3. Figures on the left side present the longitudinal stress distribution obtained in the RVE for the fiber component while the right side shows the results obtained for the matrix component. The longitudinal fiber stress distribution for the FOCH is almost uniform for both types of FE considered. While in the case of EFOCH the fiber stress distribution in the RVE is more realistic considering the bending macroscopic state. The classical linear distribution in the longitudinal stress expected for a bending load is achieved around the average value obtained for the FOCH approach. The stress distribution for the matrix present a similar behavior to the fiber component. It can be observed that the maximum stress for the fiber and matrix within the RVE are obtained in the Gauss points closest to point A, which is an expected result.

To quantify the improvement on the microscopic solution due to the EFOCH, Table 9 shows the maximum values of the longitudinal stress for the fiber and matrix components within the RVE. These stress values are graphically represented in Fig. 16 for both components. From the figures is clearly seen that the response of components change when the approach is changed.

6 Conclusions

This work presents an extension of the classical First-Order Computational Homogenization (FOCH), which has been called Enhanced-First-Order Computational Homogenization

(EFOCH). The proposed EFOCH considers the macroscopic second-order term ($\mathbf{G}$) in the microscopic displacement as the Second-Order Computational Homogenization (SOCH) does. However, the presented EFOCH conserves a first-order Boundary Value Problem (BVP) at the macroscopic scale.

As in the case of SOCH, the EFOCH obtains the same microscopic variational equilibrium equation than the FOCH (see [73]). However, the solution of the microscopic BVP must satisfy extra boundary conditions, related to the term $\mathbf{G}$. In the numerical implementation, *Periodic boundary fluctuations* condition have been imposed through the elimination of redundant unknowns method [94].

In the macroscopic BVP, the EFOCH does not take intro account the second-order stress tensor ($\hat{\mathbf{Q}}$) associated to $\mathbf{G}$ because the classical first-order formulations is preserved. Besides, the homogenized stress tensor obtained is the same than the one obtained with a FOCH due to the assumption of the symmetric materials distribution in the RVE. Because of the above, the macroscopic solution is not improved when the EFOCH is used.

However, the EFOCH is better than the FOCH from a microscopic point of view. The microscopic displacement field, the strain and the stress tensors are enhanced. The EFOCH gets a better approximation of the microscopic behavior because it takes into account the extra information provided by $\mathbf{G}$. Therefore, phenomena such as macroscopic bending or localization effect can be observed in the solution of the microscopic problem. With the proposed EFOCH, the initiation and the evolution of the non-linear performance of the microstructure will be better characterized.

Finally, it is possible to show that the FOCH is a particular case of the EFOCH. Therefore, when the principle of separation of scales is strictly verified, the results obtained using the EFOCH are the same than the ones obtained using the FOCH. In other words, if the periodic microstructural length l_μ is much smaller than the structure

characteristic length l, the contribution of $\mathbf{G}$ in the microscopic solution is negligible.

Compliance with Ethical Standards

Conflict of interest The authors declare that they have no conflict of interest.

Human and Animals Rights Statement This work does not contain any studies with human participants or animals performed by any of the authors.

Appendix: Microscopic Kinematic Relationships for the EFOCH

In the following are described the kinematic relationships defined between master and slaves nodes of the RVE, required for the implementation of the EFOCH in a FEM software.

In the Fig. 17, it is possible identify easily master nodes (named with a letter) and slave nodes (named with a letter and number). This is when a structured FE mesh on the boundary of the RVE is used. In the vertices nodes, also it is possible to identify a master node ("1") and seven slave nodes ("2","3" , ...and "8").

Using (91) is possible to write the displacement of the slave node "a_1" as a function of the displacement of the master node "a" for EFOCH as

$$\bar{\mathbf{u}}_{a_1} = \bar{\mathbf{u}}_a + D_2(\mathbf{F} - \mathbf{I}) \cdot \mathbf{N}_Y^+ + \frac{(D_2)^2}{2}\mathbf{N}_Y^+ \cdot \mathbf{G} \cdot \mathbf{N}_Y^+ \\ + D_2\mathbf{X}_a \cdot \mathbf{G} \cdot \mathbf{N}_Y^+. \tag{94}$$

To simplify the final expressions is defined

$$\mathbf{sm}_1^G = \tfrac{(D_1)^2}{2}\mathbf{N}_X^+ \cdot \mathbf{G} \cdot \mathbf{N}_X^+, \quad \mathbf{sm}_2^G = \tfrac{(D_2)^2}{2}\mathbf{N}_Y^+ \cdot \mathbf{G} \cdot \mathbf{N}_Y^+,$$
$$\mathbf{sm}_3^G = \tfrac{(D_3)^2}{2}\mathbf{N}_Z^+ \cdot \mathbf{G} \cdot \mathbf{N}_Z^+, \quad \mathbf{sm}_{12}^G = D_1 D_2 \mathbf{N}_X^+ \cdot \mathbf{G} \cdot \mathbf{N}_Y^+,$$
$$\mathbf{sm}_{13}^G = D_1 D_3 \mathbf{N}_X^+ \cdot \mathbf{G} \cdot \mathbf{N}_Z^+, \quad \mathbf{sm}_{23}^G = D_2 D_3 \mathbf{N}_Y^+ \cdot \mathbf{G} \cdot \mathbf{N}_Z^+,$$
$$\mathbf{SM}_1^G = D_1 \mathbf{N}_X^+ \cdot \mathbf{G}, \quad \mathbf{SM}_2^G = D_2 \mathbf{N}_Y^+ \cdot \mathbf{G}, \quad \mathbf{SM}_3^G = D_3 \mathbf{N}_Z^+ \cdot \mathbf{G}.$$

Therefore, it can be shown that the slaves nodes are

$$\bar{\mathbf{u}}_{a_1} = \bar{\mathbf{u}}_a + \mathbf{sm}_2 + \mathbf{sm}_2^G + \mathbf{SM}_2^G \cdot \mathbf{X}_a,$$
$$\bar{\mathbf{u}}_{a_2} = \bar{\mathbf{u}}_a + \mathbf{sm}_2 + \mathbf{sm}_3 + \mathbf{sm}_2^G + \mathbf{sm}_3^G + \mathbf{sm}_{23}^G \\ + (\mathbf{SM}_2^G + \mathbf{SM}_3^G) \cdot \mathbf{X}_a,$$
$$\bar{\mathbf{u}}_{a_3} = \bar{\mathbf{u}}_a + \mathbf{sm}_3 + \mathbf{sm}_3^G + \mathbf{SM}_3^G \cdot \mathbf{X}_a,$$
$$\bar{\mathbf{u}}_{b_1} = \bar{\mathbf{u}}_b + \mathbf{sm}_1 + \mathbf{sm}_1^G + \mathbf{SM}_1^G \cdot \mathbf{X}_b,$$
$$\bar{\mathbf{u}}_{b_2} = \bar{\mathbf{u}}_b + \mathbf{sm}_1 + \mathbf{sm}_3 + \mathbf{sm}_1^G + \mathbf{sm}_3^G + \mathbf{sm}_{13}^G \\ + (\mathbf{SM}_1^G + \mathbf{SM}_3^G) \cdot \mathbf{X}_b,$$
$$\bar{\mathbf{u}}_{b_3} = \bar{\mathbf{u}}_b + \mathbf{sm}_3 + \mathbf{sm}_3^G + \mathbf{SM}_3^G \cdot \mathbf{X}_b,$$
$$\bar{\mathbf{u}}_{c_1} = \bar{\mathbf{u}}_c + \mathbf{sm}_1 + \mathbf{sm}_1^G + \mathbf{SM}_1^G \cdot \mathbf{X}_c,$$
$$\bar{\mathbf{u}}_{c_2} = \bar{\mathbf{u}}_c + \mathbf{sm}_1 + \mathbf{sm}_2 + \mathbf{sm}_1^G + \mathbf{sm}_2^G + \mathbf{sm}_{12}^G \\ + (\mathbf{SM}_1^G + \mathbf{SM}_2^G) \cdot \mathbf{X}_c,$$
$$\bar{\mathbf{u}}_{c_3} = \bar{\mathbf{u}}_c + \mathbf{sm}_2 + \mathbf{sm}_2^G + \mathbf{SM}_2^G \cdot \mathbf{X}_c,$$
$$\bar{\mathbf{u}}_{d_1} = \bar{\mathbf{u}}_d + \mathbf{sm}_3 + \mathbf{sm}_3^G + \mathbf{SM}_3^G \cdot \mathbf{X}_d,$$
$$\bar{\mathbf{u}}_{e_1} = \bar{\mathbf{u}}_e + \mathbf{sm}_1 + \mathbf{sm}_1^G + \mathbf{SM}_1^G \cdot \mathbf{X}_e,$$
$$\bar{\mathbf{u}}_{f_1} = \bar{\mathbf{u}}_f + \mathbf{sm}_2 + \mathbf{sm}_2^G + \mathbf{SM}_2^G \cdot \mathbf{X}_f.$$

And, taking into account that the position vector of the master vertex node "1" is: $\mathbf{X}_1 = -\frac{D_1}{2}\mathbf{N}_X^+ - \frac{D_2}{2}\mathbf{N}_Y^+ - \frac{D_3}{2}\mathbf{N}_Z^+$, the slaves vertices nodes are
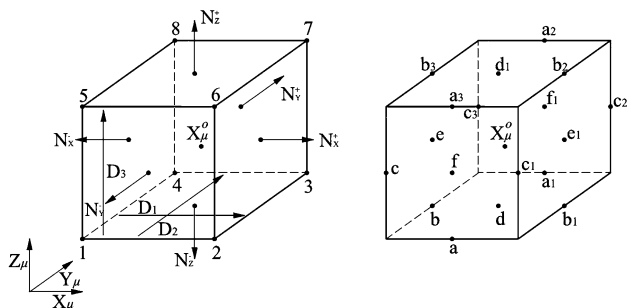
Fig. 17 Master and slaves nodes in a general hexagonal RVE
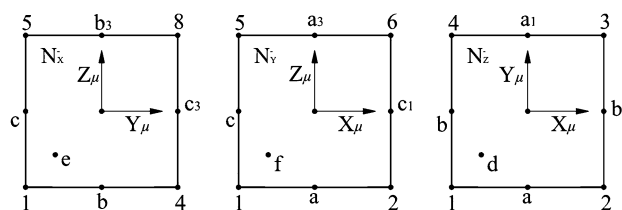
Fig. 18 Master and slaves nodes on the negative faces of the RVE

$$\bar{\mathbf{u}}_2 = \bar{\mathbf{u}}_1 + \mathbf{sm}_1 - \frac{\mathbf{sm}_{12}^G}{2} - \frac{\mathbf{sm}_{13}^G}{2},$$

$$\bar{\mathbf{u}}_3 = \bar{\mathbf{u}}_1 + \mathbf{sm}_1 + \mathbf{sm}_2 - \frac{\mathbf{sm}_{13}^G}{2} - \frac{\mathbf{sm}_{23}^G}{2},$$

$$\bar{\mathbf{u}}_4 = \bar{\mathbf{u}}_1 + \mathbf{sm}_2 - \frac{\mathbf{sm}_{12}^G}{2} - \frac{\mathbf{sm}_{23}^G}{2},$$

$$\bar{\mathbf{u}}_5 = \bar{\mathbf{u}}_1 + \mathbf{sm}_3 - \frac{\mathbf{sm}_{13}^G}{2} - \frac{\mathbf{sm}_{23}^G}{2},$$

$$\bar{\mathbf{u}}_6 = \bar{\mathbf{u}}_1 + \mathbf{sm}_1 + \mathbf{sm}_3 - \frac{\mathbf{sm}_{12}^G}{2} - \frac{\mathbf{sm}_{23}^G}{2},$$

$$\bar{\mathbf{u}}_7 = \bar{\mathbf{u}}_1 + \mathbf{sm}_1 + \mathbf{sm}_2 + \mathbf{sm}_3,$$

$$\bar{\mathbf{u}}_8 = \bar{\mathbf{u}}_1 + \mathbf{sm}_2 + \mathbf{sm}_3^G - \frac{\mathbf{sm}_{12}^G}{2} - \frac{\mathbf{sm}_{13}^G}{2}.$$

The extra boundary restrictions must be also satisfied. These boundary conditions are integral boundary constraints on each negative face of the RVE. Equation (92) can be rewritten as

$$\mathbf{A}_{yz} \cdot \bar{\mathbf{u}}_{yz} = \mathbf{H}_{yz}, in \partial \Omega_{\mu|\mathbf{N}_X^-}^h,$$

$$\mathbf{A}_{xz} \cdot \bar{\mathbf{u}}_{xz} = \mathbf{H}_{xz}, in \partial \Omega_{\mu|\mathbf{N}_Y^-}^h, \qquad (95)$$

$$\mathbf{A}_{xy} \cdot \bar{\mathbf{u}}_{xy} = \mathbf{H}_{yz}, in \partial \Omega_{\mu|\mathbf{N}_Z^-}^h$$

where,

$$\mathbf{H}_{yz} = -\frac{1}{2} D_1 D_2 D_3 (\mathbf{F} - \mathbf{I}) \cdot \mathbf{N}_X^+ + \frac{1}{8}(D_1)^2 D_2 D_3 \mathbf{G} : \mathbf{N}_X^+ \otimes \mathbf{N}_X^+$$
$$+ \frac{1}{24}(D_2)^3 D_3 \mathbf{G} : \mathbf{N}_Y^+ \otimes \mathbf{N}_Y^+ + \frac{1}{24} D_2 (D_3)^3 \mathbf{G} : \mathbf{N}_Z^+ \otimes \mathbf{N}_Z^+,$$

$$\mathbf{H}_{xz} = -\frac{1}{2} D_1 D_2 D_3 (\mathbf{F} - \mathbf{I}) \cdot \mathbf{N}_Y^+ + \frac{1}{8} D_1 (D_2)^2 D_3 \mathbf{G} : \mathbf{N}_Y^+ \otimes \mathbf{N}_Y^+$$
$$+ \frac{1}{24}(D_1)^3 D_3 \mathbf{G} : \mathbf{N}_X^+ \otimes \mathbf{N}_X^+ + \frac{1}{24} D_1 (D_3)^3 \mathbf{G} : \mathbf{N}_Z^+ \otimes \mathbf{N}_Z^+,$$

$$\mathbf{H}_{xy} = -\frac{1}{2} D_1 D_2 D_3 (\mathbf{F} - \mathbf{I}) \cdot \mathbf{N}_Z^+ + \frac{1}{8} D_1 D_2 (D_3)^2 \mathbf{G} : \mathbf{N}_Z^+ \otimes \mathbf{N}_Z^+$$
$$+ \frac{1}{24}(D_1)^3 D_2 \mathbf{G} : \mathbf{N}_X^+ \otimes \mathbf{N}_X^+ + \frac{1}{24} D_1 (D_2)^3 \mathbf{G} : \mathbf{N}_Y^+ \otimes \mathbf{N}_Y^+$$

and,

$$\mathbf{A}_{yz} = \int_{\mathbf{N}_X^-} \mathbf{N}_{yz} \, dA_{yz}, \quad \mathbf{A}_{xz} = \int_{\mathbf{N}_Y^-} \mathbf{N}_{xz} \, dA_{xz},$$

$$\mathbf{A}_{xy} = \int_{\mathbf{N}_Z^-} \mathbf{N}_{xy} \, dA_{xy}.$$

Here, $\mathbf{N}_{yz}$, $\mathbf{N}_{xz}$ and $\mathbf{N}_{xy}$ are the shape functions on the negative face YZ, XZ and XY of the RVE, respectively. And, from Fig. 18 it is possible to write the displacement vectors of the nodes on the different negative faces as

$$\bar{\mathbf{u}}_{yz} = \{\bar{\mathbf{u}}_1 | \bar{\mathbf{u}}_4 | \bar{\mathbf{u}}_5 | \bar{\mathbf{u}}_8 | \bar{\mathbf{u}}_b | \bar{\mathbf{u}}_{b_3} | \bar{\mathbf{u}}_c | \bar{\mathbf{u}}_{c_3} | \bar{\mathbf{u}}_e \},$$

$$\bar{\mathbf{u}}_{xz} = \{\bar{\mathbf{u}}_1 | \bar{\mathbf{u}}_2 | \bar{\mathbf{u}}_5 | \bar{\mathbf{u}}_6 | \bar{\mathbf{u}}_a | \bar{\mathbf{u}}_{a_3} | \bar{\mathbf{u}}_c | \bar{\mathbf{u}}_{c_1} | \bar{\mathbf{u}}_f \},$$

$$\bar{\mathbf{u}}_{xy} = \{\bar{\mathbf{u}}_1 | \bar{\mathbf{u}}_2 | \bar{\mathbf{u}}_3 | \bar{\mathbf{u}}_4 | \bar{\mathbf{u}}_a | \bar{\mathbf{u}}_{a_1} | \bar{\mathbf{u}}_b | \bar{\mathbf{u}}_{b_1} | \bar{\mathbf{u}}_d \}.$$

In the previous displacement vectors of the nodes on the negative faces of the RVE it is possible identify masters and slaves nodes. Therefore, the boundary constraints (95) obtained above can be written in terms of master nodes as

$$\mathbf{A}_{yz}^m \cdot \bar{\mathbf{u}}_{yz}^m = \mathbf{H}_{yz}^m, \ in \ \partial \Omega_{\mu|\mathbf{N}_X^-}^h,$$

$$\mathbf{A}_{xz}^m \cdot \bar{\mathbf{u}}_{xz}^m = \mathbf{H}_{xz}^m, \ in \ \partial \Omega_{\mu|\mathbf{N}_Y^-}^h, \qquad (96)$$

$$\mathbf{A}_{xy}^m \cdot \bar{\mathbf{u}}_{xy}^m = \mathbf{H}_{yz}^m, \ in \ \partial \Omega_{\mu|\mathbf{N}_Z^-}^h.$$

where,

$$\bar{\mathbf{u}}_{yz}^m = \{\bar{\mathbf{u}}_1 | \bar{\mathbf{u}}_b | \bar{\mathbf{u}}_c | \bar{\mathbf{u}}_e \},$$

$$\bar{\mathbf{u}}_{xz}^m = \{\bar{\mathbf{u}}_1 | \bar{\mathbf{u}}_a | \bar{\mathbf{u}}_c | \bar{\mathbf{u}}_f \},$$

$$\bar{\mathbf{u}}_{xy}^m = \{\bar{\mathbf{u}}_1 | \bar{\mathbf{u}}_a | \bar{\mathbf{u}}_b | \bar{\mathbf{u}}_d \}.$$

and, as an example, the term of the matrix $\mathbf{A}_{yz}^m$ for the $\bar{\mathbf{u}}_b$ of the master nodes on the negative face YZ is

$$\mathbf{A}_{yz|b}^m = \mathbf{A}_{yz|b} + \mathbf{A}_{yz|b_3}^m,$$

and the contribution to $\mathbf{H}_{yz}^m$ for the $\bar{\mathbf{u}}_{b_3}$ of the slave nodes on the negative face YZ is

$$\mathbf{H}_{yz|b}^m = \mathbf{A}_{yz|b_3}^m \cdot (\mathbf{sm}_3 + \mathbf{sm}_3^G + \mathbf{SM}_3^G \cdot \mathbf{X}_b).$$

The master nodes on the different negative faces of the RVE must verify (96). Therefore, with the aim to find redundant unknowns, it is possible to identify another slave extra node by each negative face which can be obtained as a function of the other master nodes. Then,

$$\bar{\mathbf{u}}_{yz}^{s_1} = -[\mathbf{A}_{yz}^{s_1}]^{-1} \cdot \mathbf{A}_{yz}^{(m-1)} \cdot \bar{\mathbf{u}}_{yz}^{(m-1)} + \mathbf{H}_{yz}^m, \ in \ \partial \Omega_{\mu|\mathbf{N}_X^-}^h,$$

$$\bar{\mathbf{u}}_{xz}^{s_2} = -[\mathbf{A}_{xz}^{s_2}]^{-1} \cdot \mathbf{A}_{xz}^{(m-1)} \cdot \bar{\mathbf{u}}_{xz}^{(m-1)} + \mathbf{H}_{xz}^m, \ in \ \partial \Omega_{\mu|\mathbf{N}_Y^-}^h, \quad (97)$$

$$\bar{\mathbf{u}}_{xy}^{s_3} = -[\mathbf{A}_{xy}^{s_3}]^{-1} \cdot \mathbf{A}_{xy}^{(m-1)} \cdot \bar{\mathbf{u}}_{xy}^{(m-1)} + \mathbf{H}_{yz}^m, \ in \ \partial \Omega_{\mu|\mathbf{N}_Z^-}^h.$$

References

1. Amstutz S, Giusti SM, Novotny AA, De Souza Neto EA (2010) Topological derivative for multi-scale linear elasticity models applied to the synthesis of microstructures. Int J Numer Methods Eng 84(6):733–756. doi:10.1002/nme.2922 (arXiv:1010.1724)
2. Barbero EJ (2010) Introduction to composite materials design, 2nd edn. CRC Press, Boca Raton
3. Bazant ZP (2010) Can multiscale-multiphysics methods predict softening damage and structural failure? Int J Multiscale Comput Eng 8(1):61–67. doi:10.1615/IntJMultCompEng.v8.i1.50
4. Belytschko T, Loehnert S, Song JH (2008) Multiscale aggregating discontinuities: a method for circumventing loss of material stability. Int J Numer Methods Eng 73(6):869–894. doi:10.1002/nme.2156 (arXiv:1010.1724)
5. Belytschko T, Song JH (2010) Coarse-graining of multiscale crack propagation. Int J Numer Methods Eng 81(5):537–563. doi:10.1002/nme.2694 (arXiv:1010.1724)
6. Bendsoe MP, Kikuchi N (1988) Generating optimal topologies in structural design using a homogenization method. Comput Methods Appl Mech Eng 71(2):197–224. doi:10.1016/0045-7825(88)90086-2

7. Bensoussan A, Lions J, Papanicolaou G (1978) Asymptotic analysis for periodic structures. North-Holland, Amsterdam

8. Blanco PJ, Giusti SM (2014) Thermomechanical multiscale constitutive modeling: accounting for microstructural thermal effects. J Elast 115(1):27–46. doi:10.1007/s10659-013-9445-2

9. Broughton J, Abraham F, Bernstein N, Kaxiras E (1999) Concurrent coupling of length scales: methodology and application. Phys Rev B 60(4):2391–2403. doi:10.1103/PhysRevB.60.2391

10. Budiansky B (1965) On the elastic moduli of some heterogeneous materials. J Mech Phys Solids 13(4):223–227. doi:10.1016/0022-5096(65)90011-6

11. Chatzigeorgiou G, Javili A, Steinmann P (2014) Unified magnetomechanical homogenization framework with application to magnetorheological elastomers. Math Mech Solids 19(2):193–211. doi:10.1177/1081286512458109

12. Chung PW, Tamma KK, Namburu RR (2001) Asymptotic expansion homogenization for heterogeneous media: computational issues and applications. Compos Part A Appl Sci Manuf 32(9):1291–1301. doi:10.1016/S1359-835X(01)00100-2

13. Coenen E, Kouznetsova V, Geers M (2012a) Novel boundary conditions for strain localization analyses in microstructural volume elements. Int J Numer Methods Eng 90(1):1–21. doi:10.1002/nme.3298

14. Coenen EWC, Kouznetsova VG, Geers MGD (2012b) Multi-scale continuous-discontinuous framework for computational-homogenization-localization. J Mech Phys Solids 60(8):1486–1507. doi:10.1016/j.jmps.2012.04.002

15. de Souza Neto EA, Feijóo RA (2006) Variational foundations of multi-scale constitutive models of solid: small and large strain kinematical formulation. Techinical report, LNCC research and development report, No 16. National laboratory for scientific computing, Petrópolis

16. de Souza Neto E, Feijóo R (2008) On the equivalence between spatial and material volume averaging of stress in large strain multi-scale solid constitutive models. Mech Mater 40(10):803–811. doi:10.1016/j.mechmat.2008.04.006

17. Dong JW, Feng MI (2010) Asymptotic expansion homogenization for simulating progressive damage of 3D braided composites. Compos Struct 92(4):873–882. doi:10.1016/j.compstruct.2009.09.026

18. Drugan WJ, Willis JR (1996) A micromechanics-based nonlocal constitutive equation and estimates of representative volume element size for elastic composites. J Mech Phys Solids 44(4):497–524. doi:10.1016/0022-5096(96)00007-5

19. Elmekati A, Shamy UE (2010) A practical co-simulation approach for multiscale analysis of geotechnical systems. Comput Geotech 37(4):494–503. doi:10.1016/j.compgeo.2010.02.002

20. Eshelby JD (1957) The determination of the elastic field of an ellipsoidal inclusion, and related problems. Proc R Soc A Math Phys Eng Sci 241:376–396. doi:10.1098/rspa.1957.0133

21. Ferrer A, Oliver J, Cante JC, Lloberas-Valls O (2016) Vademecum-based approach to multi-scale topological material design. Adv Model Simul Eng Sci 3(1):1–22. doi:10.1186/s40323-016-0078-4

22. Feyel F (1998) Application du calcul parallèle aux modèlles à grand nombre de variables inernes. Ph.D. thesis, Ecole des Mines de Paris

23. Feyel F (1999) Multiscale FE2 elastoviscoplastic analysis of composite structures. Comput Mater Sci 16(1–4):344–354. doi:10.1016/S0927-0256(99)00077-4

24. Feyel F (2003) A multilevel finite element method (FE2) to describe the response of highly non-linear structures using generalized continua. Comput Methods Appl Mech Eng 192(28–30):3233–3244. doi:10.1016/S0045-7825(03)00348-7

25. Feyel F, Chaboche JL (2000) FE2 multiscale approach for modelling the elastoviscoplastic behaviour of long fibre SiC/Ti composite materials. Comput Methods Appl Mech Eng 183(3–4):309–330. doi:10.1016/S0045-7825(99)00224-8

26. Fish J, Shek K, Pandheeradi M, Shephard MS (1997) Computational plasticity for composite structures based on mathematical homogenization: theory and practice. Comput Methods Appl Mech Eng 148(1–2):53–73. doi:10.1016/S0045-7825(97)00030-3

27. Fish J, Yu Q, Shek K (1999) Computational damage mechanics for composite materials based on mathematical homogenization. Int J Numer Methods Eng 45(11):1657–1679. doi:10.1002/(SICI)1097-0207(19990820)45:11<1657::AID-NME648>3.0.CO;2-H

28. Fish J, Yuan Z (2005) Multiscale enrichment based on partition of unity. Int J Numer Methods Eng 62(10):1341–1359. doi:10.1002/nme.1230

29. Geers MGD, Coenen EWC, Kouznetsova VG (2007) Multi-scale computational homogenization of structured thin sheets. Model Simul Mater Sci Eng 15(4):S393–S404. doi:10.1088/0965-0393/15/4/S06

30. Geers MGD, Kouznetsova VG, Brekelmans WAM (2010) Multi-scale computational homogenization: trends and challenges. J Comput Appl Math 234(7):2175–2182. doi:10.1016/j.cam.2009.08.077

31. Ghosh S, Lee K, Raghavan P (2001) A multi-level computational model for multi-scale damage analysis in composite and porous materials. Int J Solids Struct 38(14):2335–2385. doi:10.1016/S0020-7683(00)00167-0

32. Ghosh S, Bai J, Raghavan P (2007) Concurrent multi-level model for damage evolution in microstructurally debonding composites. Mech Mater 39(3):241–266. doi:10.1016/j.mechmat.2006.05.004

33. Gitman I, Askes H, Sluys L (2007) Representative volume: existence and size determination. Eng Fract Mech 74(16):2518–2534. doi:10.1016/j.engfracmech.2006.12.021

34. Giusti S, Blanco P, de Souza Netoo E, Feijóo R (2009) An assessment of the Gurson yield criterion by a computational multi-scale approach. Eng Comput 26(3):281–301. doi:10.1108/02644400910943626

35. González C, Segurado J, LLorca J (2004) Numerical simulation of elasto-plastic deformation of composites: evolution of stress microfields and implications for homogenization models. J Mech Phys Solids 52(7):1573–1593. doi:10.1016/j.jmps.2004.01.002

36. Guedes J, Kikuchi N (1990) Preprocessing and postprocessing for materials based on the homogenization method with adaptive finite element methods. Comput Methods Appl Mech Eng 83(2):143–198. doi:10.1016/0045-7825(90)90148-F

37. Gurson A (1977) Continuum theory of ductile rupture by void nucleation and growth: part I–yield criteria and flow rules for porous ductile media. J Eng Mater Technol 99(1):2–15. doi:10.1115/1.3443401

38. Hashin Z (1962) The elastic moduli of heterogeneous materials. J Appl Mech 29(1):143–150. doi:10.1115/1.3636446

39. Hashin Z, Shtrikman S (1962) On some variational principles in anisotropic and nonhomogeneous elasticity. J Mech Phys Solids 10(4):335–342. doi:10.1016/0022-5096(62)90004-2

40. Hashin Z, Shtrikman S (1963) A variational approach to the theory of the elastic behaviour of multiphase materials. J Mech Phys Solids 11(2):127–140. doi:10.1016/0022-5096(63)90060-7

41. Hernández J, Oliver J, Huespe A, Caicedo M, Cante J (2014) High-performance model reduction techniques in computational multiscale homogenization. Comput Methods Appl Mech Eng 276:149–189. doi:10.1016/j.cma.2014.03.011

42. Hill R (1963) Elastic properties of reinforced solids: some theoretical principles. J Mech Phys Solids 11(5):357–372. doi:10.1016/0022-5096(63)90036-X

43. Hill R (1965a) A self-consistent mechanics of composite materials. J Mech Phys Solids 13(4):213–222. doi:10.1016/0022-5096(65)90010-4

44. Hill R (1965b) Continuum micro-mechanics of elastoplastic polycrystals. J Mech Phys Solids 13(2):89–101. doi:10.1016/0022-5096(65)90023-2

45. Hill R (1972) On constitutive macro-variables for heterogeneous solids at finite strain. Proc R Soc Lond A 326(1565):131–147. doi:10.1098/rspa.1972.0001

46. Hill R (1984) On macroscopic effects of heterogeneity in elastoplastic media at finite strain. Math Proc Camb Philos Soc 95(03):481. doi:10.1017/S0305004100061818

47. Hund A, Ramm E (2007) Locality constraints within multiscale model for non-linear material behaviour. Int J Numer Methods Eng 70(13):1613–1632. doi:10.1002/nme.1953

48. Ilic S, Hackl K (2009) Application of the multiscale FEM to the modeling of nonlinear multiphase materials. J Theor Appl Mech 47(3):537–551

49. Javili A, Chatzigeorgiou G, Steinmann P (2013) Computational homogenization in magneto-mechanics. Int J Solids Struct 50(25–26):4197–4216. doi:10.1016/j.ijsolstr.2013.08.024

50. Kaczmarczyk L, Pearce CJ, Bićanić N (2008) Scale transition and enforcement of RVE boundary conditions in second-order computational homogenization. Int J Numer Methods Eng 74(3):506–522. doi:10.1002/nme.2188

51. Kalamkarov AL, Andrianov IV, Danishevs'kyy VV (2009) Asymptotic homogenization of composite materials and structures. Appl Mech Rev 62(3):030,802, doi:10.1115/1.3090830, arXiv:77950863481

52. Kanit T, N'Guyen F, Forest S, Jeulin D, Reed M, Singleton S (2006) Apparent and effective physical properties of heterogeneous materials: representativity of samples of two materials from food industry. Comput Methods Appl Mech Eng 195(33–36):3960–3982. doi:10.1016/j.cma.2005.07.022

53. Kanit T, Forest S, Galliet I, Mounoury V, Jeulin D (2003) Determination of the size of the representative volume element for random composites: statistical and numerical approach. Int J Solids Struct 40(13–14):3647–3679. doi:10.1016/S0020-7683(03)00143-4

54. Kanouté P, Boso DP, Chaboche JL, Schrefler BA (2009) Multiscale methods for composites: a review. Arch Comput Methods Eng 16(1):31–75. doi:10.1007/s11831-008-9028-8

55. Kato J, Yachi D, Terada K, Kyoya T (2014) Topology optimization of micro-structure for composites applying a decoupling multi-scale analysis. Struct Multidiscip Optim 49(4):595–608. doi:10.1007/s00158-013-0994-6

56. Keip MA, Steinmann P, Schröder J (2014) Two-scale computational homogenization of electro-elasticity at finite strains. Comput Methods Appl Mech Eng 278:62–79. doi:10.1016/j.cma.2014.04.020

57. Klinge S, Hackl K (2012) Application of the multiscale fem to the modeling of nonlinear composites with a random microstructure. Int J Multiscale Comput Eng 10(3):213–227. doi:10.1615/IntJMultCompEng.002059

58. Kouznetsova VG (2002) Computational homogenization for the multi-scale analysis of multi-phase materials. Ph.D. thesis, Eindhoven University of Technology, Eindhoven, The Netherlands

59. Kouznetsova V, Brekelmans WAM, Baaijens FPT (2001) Approach to micro-macro modeling of heterogeneous materials. Comput Mech 27(1):37–48. doi:10.1007/s004660000212

60. Kouznetsova V, Geers MGD, Brekelmans WAM (2002) Multi-scale constitutive modelling of heterogeneous materials with a gradient-enhanced computational homogenization scheme. Int J Numer Methods Eng 54(8):1235–1260. doi:10.1002/nme.541

61. Kouznetsova VG, Geers MGD, Brekelmans WAM (2004) Multi-scale second-order computational homogenization of multi-phase materials: a nested finite element solution strategy. Comput Methods Appl Mech Eng 193(48–51):5525–5550. doi:10.1016/j.cma.2003.12.073

62. Ladevèze P, Loiseau O, Dureisseix D (2001) A micro-macro and parallel computational strategy for highly heterogeneous structures. Int J Numer Methods Eng 52(12):121–138. doi:10.1002/nme.274

63. Lahellec N, Suquet P (2007) On the effective behavior of nonlinear inelastic composites: I. Incremental variational principles. J Mech Phys Solids 55(9):1932–1963. doi:10.1016/j.jmps.2007.02.003

64. Lamari H, Ammar A, Cartraud P, Legrain G, Chinesta F, Jacquemin F (2010) Routes for efficient computational homogenization of nonlinear materials using the proper generalized decompositions. Arch Comput Methods Eng 17(4):373–391. doi:10.1007/s11831-010-9051-4

65. Larsson R, Diebels S (2007) A second-order homogenization procedure for multi-scale analysis based on micropolar kinematics. Int J Numer Methods Eng 69(12):2485–2512. doi:10.1002/nme.1854. arXiv:1010.1724

66. Larsson R, Zhang Y (2007) Homogenization of microsystem interconnects based on micropolar theory and discontinuous kinematics. J Mech Phys Solids 55(4):819–841. doi:10.1016/j.jmps.2006.09.010

67. Lloberas-Valls O, Rixen D, Simone A, Sluys L (2012) On micro-to-macro connections in domain decomposition multiscale methods. Comput Methods Appl Mech Eng 225:177–196. doi:10.1016/j.cma.2012.03.022

68. Mandel J (1971) Plasticité Classique Et Viscoplasticité. International Centre for Mechanical Sciences. Courses and lectures, Springer, Udine, https://books.google.es/books?id=zvHaoAEACAAJ

69. Matsui K, Terada K, Yuge K (2004) Two-scale finite element analysis of heterogeneous solids with periodic microstructures. Comput Struct 82(7–8):593–606. doi:10.1016/j.compstruc.2004.01.004

70. McDowell DL (2010) A perspective on trends in multiscale plasticity. Int J Plast 26(9):1280–1309. doi:10.1016/j.ijplas.2010.02.008

71. Melro A, Camanho P, Pinho S (2012) Influence of geometrical parameters on the elastic response of unidirectional composite materials. Compos Struct 94(11):3223–3231. doi:10.1016/j.compstruct.2012.05.004

72. Michel J, Moulinec H, Suquet P (1999) Effective properties of composite materials with periodic microstructure: a computational approach. Comput Methods Appl Mech Eng 172(1–4):109–143. doi:10.1016/S0045-7825(98)00227-8

73. Miehe C, Schröder J, Schotte J (1999) Computational homogenization analysis in finite plasticity Simulation of texture development in polycrystalline materials. Comput Methods Appl Mech Eng 171(3–4):387–418. doi:10.1016/S0045-7825(98)00218-7

74. Miehe C (2002) Strain-driven homogenization of inelastic microstructures and composites based on an incremental variational formulation. Int J Numer Methods Eng 55(11):1285–1322. doi:10.1002/nme.515

75. Miehe C, Schröder J, Bayreuther C (2002) On the homogenization analysis of composite materials based on discretized fluctuations on the micro-structure. Acta Mech 155(1–2):1–16. doi:10.1007/BF01170836

76. Miehe C, Dettmar J, Zäh D (2010) Homogenization and two-scale simulations of granular materials for different

microstructural constraints. Int J Numer Methods Eng 83(8–9):1206–1236. doi:10.1002/nme.2875

77. Miehe C, Vallicotti D, Teichtmeister S (2016) Homogenization and multiscale stability analysis in finite magneto-electro-elasticity. Application to soft matter EE, ME and MEE composites. Comput Methods Appl Mech Eng 300:294–346. doi:10.1016/j.cma.2015.10.013

78. Miehe C, Koch A (2002) Computational micro-to-macro transitions of discretized microstructures undergoing small strains. Arch Appl Mech 72(4–5):300–317. doi:10.1007/s00419-002-0212-2

79. Monteiro E, Yvonnet J, He Q (2008) Computational homogenization for nonlinear conduction in heterogeneous materials using model reduction. Comput Mater Sci 42(4):704–712. doi:10.1016/j.commatsci.2007.11.001

80. Mosby M, Matouš K (2015) Hierarchically parallel coupled finite strain multiscale solver for modeling heterogeneous layers. Int J Numer Methods Eng 102(3–4):748–765. doi:10.1002/nme.4755

81. Nemat-Nasser S (1999a) Averaging theorems in finite deformation plasticity. Mech Mater 31(8):493–523. doi:10.1016/S0167-6636(98)00073-8

82. Nemat-Nasser S (1999b) Averaging theorems in finite deformation plasticity. Mech Mater 31(8):493–523. doi:10.1016/S0167-6636(98)00073-8

83. Nguyen VPHU, Stroeven M, Sluys LJ (2011) Multiscale continuous and discontinuous modeling of heterogeneous materials : a review on recent developments. J Multiscale Model 3(4):1–42. doi:10.1142/S1756973711000509

84. Oden JT, Vemaganti K, Moës N (1999) Hierarchical modeling of heterogeneous solids. Comput Methods Appl Mech Eng 172(1):3–25. doi:10.1016/S0045-7825(98)00224-2

85. Oliver J (1996) Modelling strong discontinuities in solid mechanics via strain softening constitutive equations. Part 1: fundamentals. Int J Numer Methods Eng 39(21):3575–3600. doi:10.1002/(SICI)1097-0207(19961115)39:21<3575::AID-NME65>3.0.CO;2-E

86. Oliver J, Caicedo M, Roubin E, Huespe AE, Hernández JA (2015) Continuum approach to computational multiscale modeling of propagating fracture. Comput Methods Appl Mech Eng 294:384–427. doi:10.1016/j.cma.2015.05.012

87. Oliver J, Huespe AE (2004a) Continuum approach to material failure in strong discontinuity settings. Comput Methods Appl Mech Eng 193(30–32):3195–3220. doi:10.1016/j.cma.2003.07.013

88. Oliver J, Huespe AE (2004b) Theoretical and computational issues in modelling material failure in strong discontinuity scenarios. Comput Methods Appl Mech Eng 193(27–29):2987–3014. doi:10.1016/j.cma.2003.08.007

89. Oller S, Miquel Canet J, Zalamea F (2005) Composite material behavior using a homogenization double scale method. J Eng Mech 131(1):65–79. doi:10.1061/(ASCE)0733-9399(2005)131:1(65)

90. Ostoja-Starzewski M (2002) Microstructural randomness versus representative volume element in thermomechanics. J Appl Mech 69(1):25–35. doi:10.1115/1.1410366

91. Ostoja-Starzewski M (2006) Material spatial randomness: from statistical to representative volume element. Probab Eng Mech 21(2):112–132. doi:10.1016/j.probengmech.2005.07.007

92. Otero F (2016) Multiscale numerical modelling of microstructured reinforced composites. Ph.D. thesis, Universitat Politècnica de Catalunya (BarcelonaTECH). doi:10.13140/RG.2.1.5155.5600

93. Otero F, Martinez X, Oller S, Salomón O (2015) An efficient multi-scale method for non-linear analysis of composite structures. Compos Struct 131:707–719. doi:10.1016/j.compstruct.2015.06.006

94. Otero F, Oller S, Martinez X, Salomón O (2015b) Numerical homogenization for composite materials analysis. Comparison with other micro mechanical formulations. Compos Struct 122:405–416. doi:10.1016/j.compstruct.2014.11.041

95. Özdemir I, Brekelmans WAM, Geers MGD (2008) FE2 computational homogenization for the thermo-mechanical analysis of heterogeneous solids. Comput Methods Appl Mech Eng 198(3–4):602–613. doi:10.1016/j.cma.2008.09.008

96. Pérez MA, Martínez X, Oller S, Gil L, Rastellini F, Flores F (2013) Impact damage prediction in carbon fiber-reinforced laminated composite using the matrix-reinforced mixing theory. Compos Struct 104:239–248. doi:10.1016/j.compstruct.2013.04.021

97. Perić D, de Souza Neto EA, Feijóo RA, Partovi M, Molina AJC (2011) On micro-to-macro transitions for multi-scale analysis of non-linear heterogeneous materials: unified variational basis and finite element implementation. Int J Numer Methods Eng 87(1–5):149–170. doi:10.1002/nme.3014

98. Pinho-da Cruz J, Oliveira J, Teixeira-Dias F (2009) Asymptotic homogenisation in linear elasticity. Part I: mathematical formulation and finite element modelling. Comput Mater Sci 45(4):1073–1080. doi:10.1016/j.commatsci.2009.02.025

99. PLCd research group (1991-to present) PLCd: Non-linear thermo-mechanic finite element code for research-oriented applications. Free access code developed at CIMNE. http://www.cimne.com/PLCd

100. Reis FJP, Andrade Pires FM (2013) An adaptive sub-incremental strategy for the solution of homogenization-based multiscale problems. Comput Methods Appl Mech Eng 257:164–182. doi:10.1016/j.cma.2013.01.003

101. Renard J, Marmonier MF (1987) Etude de l'initiation de l'endommagement dans la matrice d'un matériau composite par une méthode d'homogénéisation. Aerosp Sci Technol 6:37–51

102. Sanchez-Palencia E (1980) Non-homogeneous media and vibration theory. In: Lecture Notes in Physics, Lecture Notes in Physics, vol 127, Springer, Berlin, Heidelberg. doi:10.1007/3-540-10000-8

103. Sanchez-Palencia E (1983) Homogenization method for the study of composite media. In: Verhulst F (ed) Asymptotic analysis II, Lecture Notes in mathematics, vol 985, Springer, Berlin, Heidelberg, pp 192–214. doi:10.1007/BFb0062368

104. Schröder J (2009) Derivation of the localization and homogenization conditions for electro-mechanically coupled problems. Comput Mater Sci 46(3):595–599. doi:10.1016/j.commatsci.2009.03.035

105. Schröder J (2014) A numerical two-scale homogenization scheme: the FE2-method. In: Plasticity and Beyond: Microstructures, Crystal-Plasticity and Phase Transitions, vol 550, pp 1–64. doi:10.1007/978-3-7091-1625-8_1

106. Schury F, Stingl M, Wein F (2012) Efficient two-scale optimization of manufacturable graded structures. SIAM J Sci Comput 34(6):B711–B733. doi:10.1137/110850335

107. Segurado J, Llorca J (2002) A numerical approximation to the elastic properties of sphere-reinforced composites. J Mech Phys Solids 50(10):2107–2121. doi:10.1016/S0022-5096(02)00021-2

108. Smit R, Brekelmans W, Meijer H (1998) Prediction of the mechanical behavior of nonlinear heterogeneous systems by multi-level finite element modeling. Comput Methods Appl Mech Eng 155(1–2):181–192. doi:10.1016/S0045-7825(97)00139-4

109. Smit R, Brekelmans W, Meijer H (1999) Prediction of the large-strain mechanical response of heterogeneous polymer systems: local and global deformation behaviour of a representative

volume element of voided polycarbonate. J Mech Phys Solids 47(2):201–221. doi:10.1016/S0022-5096(98)00089-1

110. Somer DD, de Souza Neto EA, Dettmer WG, Perić D (2009) A sub-stepping scheme for multi-scale analysis of solids. Comput Methods Appl Mech Eng 198(9–12):1006–1016. doi:10.1016/j.cma.2008.11.013

111. Song JH, Belytschko T (2009) Multiscale aggregating discontinuities method for micro-macro failure of composites. Compos Part B Eng 40(6):417–426. doi:10.1016/j.compositesb.2009.01.007

112. Sunyk R, Steinmann P (2003) On higher gradients in continuum-atomistic modelling. Int J Solids Struct 40(24):6877–6896. doi:10.1016/j.ijsolstr.2003.07.001

113. Suquet PM (1985) Local and global aspects in the mathematical theory of plasticity. In: Sawczuk A, Bianchi G (eds) Plasticity today—modeling methods and applications. Elsevier, London, pp 279–310

114. Swan CC (1994) Techniques for stress- and strain-controlled homogenization of inelastic periodic composites. Comput Methods Appl Mech Eng 117(3–4):249–267. doi:10.1016/0045-7825(94)90117-1

115. Takano N, Ohnishi Y, Zako M, Nishiyabu K (2000) The formulation of homogenization method applied to large deformation problem for composite materials. Int J Solids 37(44):6517–6535. doi:10.1016/S0020-7683(99)00284-X

116. Temizer I (2012) On the asymptotic expansion treatment of two-scale finite thermoelasticity. Int J Eng Sci 53:74–84. doi:10.1016/j.ijengsci.2012.01.003

117. Temizer I, Wriggers P (2011a) An adaptive multiscale resolution strategy for the finite deformation analysis of micro-heterogeneous structures. Comput Methods Appl Mech Eng 200(37):2639–2661. doi:10.1016/j.cma.2010.06.013

118. Temizer I, Wriggers P (2011b) Homogenization in finite thermoelasticity. J Mech Phys Solids 59(2):344–372. doi:10.1016/j.jmps.2010.10.004

119. Temizer I, Zohdi TI (2007) A numerical method for homogenization in non-linear elasticity. Comput Mech 40(2):281–298. doi:10.1007/s00466-006-0097-y

120. Terada K, Hori M, Kyoya T, Kikuchi N (2000) Simulation of the multi-scale convergence in computational homogenization approaches. Int J Solids Struct 37(16):2285–2311. doi:10.1016/S0020-7683(98)00341-2

121. Terada K, Saiki I, Matsui K, Yamakawa Y (2003) Two-scale kinematics and linearization for simultaneous two-scale analysis of periodic heterogeneous solids at finite strain. Comput Methods Appl Mech Eng 192(31–32):3531–3563. doi:10.1016/S0045-7825(03)00365-7

122. Terada K, Kurumatani M, Ushida T, Kikuchi N (2010) A method of two-scale thermo-mechanical analysis for porous solids with micro-scale heat transfer. Comput Mech 46(2):269–285. doi:10.1007/s00466-009-0400-9

123. Terada K, Kikuchi N (2001) A class of general algorithms for multi-scale analyses of heterogeneous media. Comput Methods Appl Mech Eng 190(40–41):5427–5464. doi:10.1016/S0045-7825(01)00179-7

124. Unger JF (2013) An FE2-X1 approach for multiscale localization phenomena. J Mech Phys Solids 61(4):928–948. doi:10.1016/j.jmps.2012.12.010

125. van der Sluis O, Schreurs PJG, Meijer HEH (1999) Effective properties of a viscoplastic constitutive model obtained by homogenization. Mech Mater 31(11):743–759. doi:10.1016/S0167-6636(99)00028-9

126. van der Sluis O, Schreurs P, Brekelmans W, Meijer H (2000) Overall behaviour of heterogeneous elastoviscoplastic materials: effect of microstructural modelling. Mech Mater 32(8):449–462. doi:10.1016/S0167-6636(00)00019-3

127. Wellmann C, Wriggers P (2012) A two-scale model of granular materials. Comput Methods Appl Mech Eng 205:46–58. doi:10.1016/j.cma.2010.12.023

128. Xia L, Breitkopf P (2014) Concurrent topology optimization design of material and structure within FE2 nonlinear multiscale analysis framework. Comput Methods Appl Mech Eng 278:524–542. doi:10.1016/j.cma.2014.05.022

129. Yvonnet J, He QC (2007) The reduced model multiscale method (R3M) for the non-linear homogenization of hyperelastic media at finite strains. J Comput Phys 223(1):341–368. doi:10.1016/j.jcp.2006.09.019